Paleoceanography and Paleoclimatology

RESEARCH ARTICLE
10.1029/2022PA004424

Multiproxy Reconstruction of Pliocene North Atlantic Sea Surface Temperatures and Implications for Rainfall in North Africa

J. B. Wycech[1], B. Rajagopalan[1,2], P. H. Molnar[1,3], E. Gill[4], and T. M. Marchitto[3,5]

[1]Cooperative Institute for Research in Environmental Sciences, Boulder, CO, USA, [2]Department of Civil, Environmental and Architectural Engineering, University of Colorado, Boulder, CO, USA, [3]Department of Geological Sciences, University of Colorado, Boulder, CO, USA, [4]Zillow Group, Seattle, WA, USA, [5]Institute of Arctic and Alpine Research, University of Colorado, Boulder, CO, USA

Abstract Wetter conditions in the African Sahel during the Pliocene (5.3–2.6 Ma) likely played an important role in hominid evolution and may be explained by warm North Atlantic sea-surface temperatures (SSTs), similar to the modern warm phase of the Atlantic multidecadal oscillation (AMO). We reconstruct Pliocene North Atlantic (2°S to 60°N) SSTs through a multiproxy reduced-dimension methodology that combines two new foraminiferal (*Trilobatus sacculifer*) Mg/Ca-based SST records from Ocean Drilling Program sites in the northwestern Atlantic (Site 997) and Gulf of Mexico (Site 625) with previously published multi-proxy SST records from seven additional Atlantic sites. Our Pliocene reconstructions indicate that the North Atlantic was overall warmer than the comparison period (0–0.5 Ma) with the most extreme warming occurring in the tropical and eastern subtropical North Atlantic and in the Labrador Sea. Furthermore, the mean state of North Atlantic warming at 5 Ma resembles that of the modern warm phase of the AMO with average SST anomalies of 3.8°C ± 0.5°C in the AMO region. With that reconstructed index, along with reconstructed El Niño-like eastern Tropical Pacific SSTs from our previous research, we reconstruct rainfall over the Pliocene North Africa, covering the Sahara-Sahel region and the Megalake Chad Basin and find up to twice the rainfall of that today. We surmise that this increased precipitation rate, along with other aiding land and sub-surface processes, sustained Megalake Chad.

Plain Language Summary Reconstruction of climate conditions during the Pliocene (5.3–2.6 million years ago) is considered to be a useful indicator of conditions expected by the end of the 21st century as it is the most recent interval in Earth history when the atmosphere's carbon dioxide concentrations may have been comparable to today. Shoreline reconstructions of paleo-Lake Chad in the African Sahel indicate that wetter-than-modern conditions prevailed during the Pliocene. Today, rainfall in the Sahel responds to periodic increases in North Atlantic sea surface temperatures, a phenomenon known as Atlantic multidecadal oscillation (AMO), and to the tropical Pacific phenomenon known as El Niño Southern Oscillation (ENSO). In this study, we compiled 9 Pliocene sea-surface temperature (SST) records across the North Atlantic (2°S–60°N) and applied a statistical method to create detailed SST maps. Our maps reveal that the region was warmer than today, with warming similar to that observed for the warm phase of modern AMO. Using our reconstructions of North Atlantic SSTs and ENSO indices, we infer a wetter Pliocene Sahara-Sahel region. We estimate that North Africa and the Megalake Chad Basin were up to twice as wet as today, which was instrumental in sustaining the enormous lake.

Key Points:

- Pliocene North Atlantic sea surface temperatures were warmer than modern with largest differences in the subpolar north
- Sea surface temperature anomalies resemble those of a modern warm Atlantic multidecadal oscillation phase
- Based on the reconstructed sea surface temperatures, the Pliocene African Sahel rainfall is estimated to be nearly twice that of modern

Supporting Information:

Supporting Information may be found in the online version of this article.

Correspondence to:

J. B. Wycech,
jody.wycech@colorado.edu

Citation:

Wycech, J. B., Rajagopalan, B., Molnar, P. H., Gill, E., & Marchitto, T. M. (2022). Multiproxy reconstruction of Pliocene North Atlantic sea surface temperatures and implications for rainfall in North Africa. *Paleoceanography and Paleoclimatology*, *37*, e2022PA004424. https://doi.org/10.1029/2022PA004424

Received 6 FEB 2022
Accepted 11 DEC 2022

Author Contributions:

Conceptualization: B. Rajagopalan, P. H. Molnar
Data curation: J. B. Wycech
Formal analysis: J. B. Wycech, T. M. Marchitto
Funding acquisition: J. B. Wycech, B. Rajagopalan, P. H. Molnar, T. M. Marchitto
Investigation: J. B. Wycech, B. Rajagopalan, P. H. Molnar, T. M. Marchitto
Methodology: J. B. Wycech, B. Rajagopalan, P. H. Molnar
Project Administration: B. Rajagopalan, T. M. Marchitto
Resources: B. Rajagopalan, P. H. Molnar, T. M. Marchitto
Software: J. B. Wycech, B. Rajagopalan, E. Gill

1. Introduction

The Pliocene Epoch attracts paleoclimatologists both because of its apparent climatic similarities with predictions of future, 21st century climate, and because the boundary conditions that differ from those of today, including less ice and wetter subtropical land surfaces, pose challenges to understanding the Pliocene. Approaches to better understanding have largely followed one of two approaches: calculations using general circulation models (GCMs) with boundary conditions assumed appropriate for Pliocene time (e.g., Barreiro et al., 2006; Burls & Fedorov, 2017; Chandan & Peltier, 2018; Chandler et al., 1994; Dowsett et al., 2012; Fedorov et al., 2006; Haywood et al., 2020; Vizcaíno et al., 2010; Zhang et al., 2021), and exploitation of modern climatic patterns as prototypes for longer-term background conditions, an approach that follows the geological mantra that "the present is the key

Supervision: B. Rajagopalan, P. H. Molnar, T. M. Marchitto
Validation: J. B. Wycech
Visualization: J. B. Wycech
Writing – original draft: J. B. Wycech, P. H. Molnar
Writing – review & editing: J. B. Wycech, B. Rajagopalan, P. H. Molnar, E. Gill, T. M. Marchitto

to the past." The latter approach is illustrated well by inferred relationships between past sea-surface temperatures (SSTs) in the equatorial Pacific (e.g., Kienast et al., 2006; Koutavas et al., 2006; Martínez et al., 2003; Pahnke et al., 2007) and changes in climates in surrounding regions. Specifically, the transition from cool mid-Holocene SSTs in the tropical Pacific, which are typical of La Niña conditions, to warmer conditions and more El Niño events (e.g., Carré et al., 2014; Clement et al., 2000; Sandweiss et al., 1996, 2009) offers explanations for transitions from fewer to more frequent heavy rainfall events over the Andes (e.g., Moy et al., 2002; Rodbell et al., 1999), and for changing amounts and intensity of precipitation in the southeastern (Donders et al., 2005), midwestern (e.g., Knox, 2000), and southwestern USA (e.g., Ely, 1997; Ely et al., 1993). We have previously followed this latter approach of treating present-day teleconnections as templates for understanding past climate (e.g., Gill et al., 2016, 2017; Molnar & Cane, 2002, 2007; Molnar & Rajagopalan, 2012, 2020; Wycech et al., 2020), and we do so again here. Our target is SST variation over the North Atlantic since 5 Ma, and possible impacts of those changing SSTs on African rainfall.

Both approaches have obvious virtues, but both have limitations. GCM runs depend on numerous assumptions, not just those that characterize differences between Pliocene and present-day conditions, but also assumed parameterizations that lead to different temperatures, precipitation, etc. among the models. Large differences of, for example, 2°C–5°C among mid-Pliocene mean global temperatures calculated with different GCMs demonstrates the effects of different parameterizations (e.g., Haywood et al., 2020). Regarding present-day teleconnections, some seem to apply both to annual cycles and to more permanent conditions as shown by GCMs results (e.g., Barreiro et al., 2006; Shukla et al., 2011; Vizcaíno et al., 2010), but others ought not. For example, El Niño events commonly send coastally trapped Kelvin waves northward along the west coast of North America that lead to transient warming (e.g., Collins et al., 2002; Frischknecht et al., 2015; Nezlin & McWilliams, 2003), but obviously, such transients will not characterize a multiyear, let alone a millennial, climate that includes a millennial to million-year warm eastern tropical Pacific ("permanent El Niño"). Just as modern climate includes transients that may be absent in long-term climate basic states, modern climate also does not sample some extremes between present-day and past climates. For example, the nearly 10°C differences between Pliocene and present-day SSTs along eastern boundary currents, like the California and Benguela Currents (e.g., Dekens et al., 2007; Marlow et al., 2000), are absent from modern variability; thus, replicating them using modern climate variability as a template will likely provide inaccurate results. Although short-term weather events seem necessary to sustain upwelling of cold deep water and cool SSTs (e.g., Li et al., 2019; Miller & Tziperman, 2017), the apparent absence of such localized regions of cold water seems to depend on weaker Pliocene zonal pressure gradients across these currents (Arnold & Tziperman, 2015), presumably due to wetter adjacent continental regions than occur in present-day climate (e.g., Fu et al., 2021).

Modern North Atlantic climate is often characterized by a few quantities that describe regional patterns, or modes, like the El Niño Southern Oscillation (ENSO) NINO3.4 index in the equatorial Pacific. The North Atlantic Oscillation, commonly parametrized by the pressure difference between Iceland and Iberia or the Azores (e.g., Hurrell et al., 2003), characterizes much variability of the atmosphere (e.g., Hurrell & Deser, 1997; Marshall et al., 2001; Thompson et al., 2003), but as our focus is on SSTs, we do not exploit it. Among quantities that we reference is the "Atlantic multidecadal oscillation," or AMO, which Enfield et al. (2001) defined as the decadal mean temperature anomaly averaged over the North Atlantic north of the equator. Although such a feature could be obscured by background global warming, removal of that global warming signal leaves a clear AMO signal (Wills et al., 2019). The decadal aspect of the AMO reduces the risk of treating annual transients, like coastal Kelvin waves generated by El Niño events mentioned above, as features with million-year durations. Moreover, correlations with the AMO of decadal variability of climates elsewhere are clear, such as in displacements of Intertropical Convergence Zone (Green et al., 2017), rainfall over Eurasia and the Sahel, and Indian monsoon rainfall (e.g., Folland et al., 1986; Liu & Chiang, 2012; Zhang & Delworth, 2006). Related to Sahel rainfall, a warmer North Atlantic (a warm AMO phase) is typically coupled with a cooler tropical south Atlantic, which increases the cross-equatorial temperature gradient and consequently, the west African Monsoon (Berntell et al., 2018; Martin et al., 2014; Molnar & Rajagopalan, 2020 and references therein). Deepening of this low-pressure zone enhances the gradient and thus monsoon strength. The observed relationship between short-lived climate oscillations, such as ENSO or AMO, with rainfall in distal regions in the modern motivates the application of such correlations to longer time scales such as the Pliocene.

We pursue SSTs over the North Atlantic (2°S–60°N) since 5 Ma, using the same approach used in recent studies (e.g., Gill et al., 2016, 2017; Tierney et al., 2019; Wycech et al., 2020). We reduce modern monthly variability

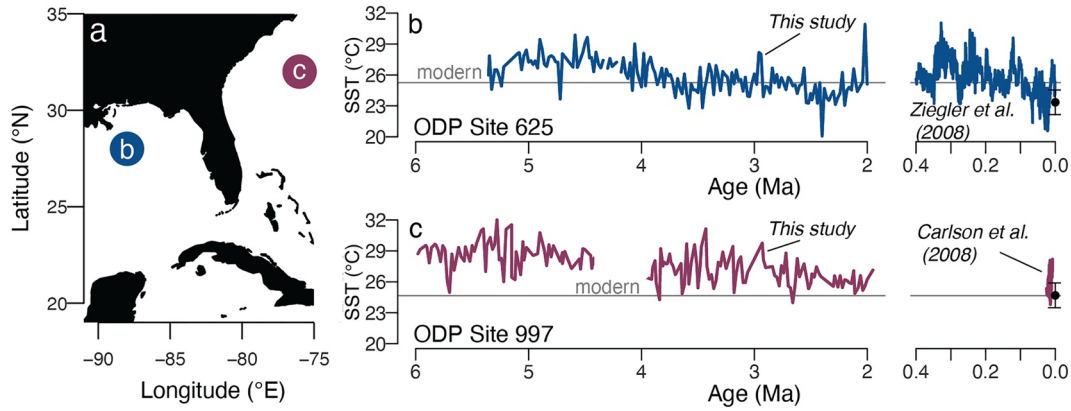

Figure 1. Summary of Northwest Atlantic Plio-Pleistocene Mg/Ca-based sea-surface temperature (SST) records. Mg/Ca ratios were obtained from *Trilobatus sacculifer* (this study, >2 Ma) and from *Globigerinoides ruber* (previous studies, <0.4 Ma) and are converted to SST as described in Section 2.1. (a) Map showing locations of the SST records shown in panels (b) and (c). (b) SST record for Ocean Drilling Program (ODP) Site 625 from this study (5.35–2 Ma) and Ziegler et al. (2008) (0.4–0 Ma). (c) Blake Ridge SST records from this study (6–1.95 Ma, ODP Site 997) and Carlson et al. (2008) (0–25 ka, nearby KNR140-51GGC). Dashed gray horizontal line marks modern SST at each site (see Section 4.1 for details). Black points note core top SST derived from *T. sacculifer* Mg/Ca ratios (this study), error bars are Mg/Ca calibration error (±1.2°C SE; Anand et al., 2003; Dekens et al., 2002).

to the sum of four empirical orthogonal eigen functions that characterize "full field" spatial patterns, at 2° × 2°, with separate time series for each. We then carry out the same analysis but using data only from points where paleo-SSTs have been measured (the "limited field"), which facilitates a "reduced-dimension methodology." Using a least-squares fit of reduced-dimension eigenvalues to those of the full field pattern, we estimate weights that we can apply to past SSTs, which have been sampled at only nine sites, to estimate past SSTs for the North Atlantic. Then using reconstructed SSTs since 5 Ma and the spatial definition of the AMO, we offer a history of mean SSTs in the region (i.e., an AMO-like index, averaged over millennia). As an ultimate goal is to understand differences between Pliocene and present-day climates, we then use correlations of the AMO and ENSO in modern climate with African rainfall to estimate differences between past and present-day rainfall over the region surrounding Lake Chad that today is renowned for marked aridity. In Pliocene time, Megalake Chad was a huge lake that drained into the Mediterranean; we argue that the warmer Atlantic facilitated greater rainfall over the Megalake Chad region.

2. Data

2.1. New Plio-Pleistocene SST Records From the Northwest Atlantic

One technique commonly used to reconstruct paleo-SSTs exploits the Mg/Ca ratio of foraminifer calcite, which increases exponentially with increasing temperature as demonstrated by culturing experiments performed on living species (e.g., Allen et al., 2016; Lea et al., 1999; Nürnberg et al., 1996). We used this approach to generate two new Pliocene SST records from the Mg/Ca ratios of the mixed-layer dwelling foraminifer species *Trilobatus sacculifer* (Spezzaferri et al., 2015) recovered from Ocean Drilling Program (ODP) sites 625 and 997 in the Gulf of Mexico and Northwest Atlantic, respectively (Figure 1a). These records were generated to increase Pliocene SST data around the Southeastern United States—an area that is sensitive to modern AMO teleconnections (Enfield et al., 2001).

ODP Site 625 is in the Gulf of Mexico (28.832°N, 87.160°W, 900 m water depth) proximal to the modern Mississippi River Delta (Rabinowitz et al., 1985). The Site 625 Pliocene section has been constrained by astrochronologic tuning and biostratigraphy (Joyce et al., 1990), which served as guide for sample selection. A total of 158 Pliocene-aged samples were selected spanning 2.001–5.355 Ma with a sampling resolution varying between 8 and 129 kyr (mean = 22 kyr) or 30–489 cm (mean = 81 cm). One Holocene-aged sample was also selected (0.13–0.15 m below sea floor, mbsf) for a Pliocene-Holocene data comparison.

ODP Site 997 is on the Blake Ridge in the Northwest Atlantic (31.843°N, 75.468°W, 2,770 m water depth; Paull et al., 1996). Temporal constraints for the Pliocene section are based on nannofossil biostratigraphy (Okada, 2000). A total of 152 Pliocene-aged samples were selected spanning 1.95–5.98 Ma with a sampling resolution varying between less than 1 kyr to 510 kyrs (mean = 27 kyrs) or 22 cm–21.8 m (mean = 340 cm). One Holocene-aged core top sample (0 mbsf) was also analyzed from Site 997.

Prior to foraminifer identification and analysis, each core sample was disaggregated using a pH-buffered hydrogen peroxide sodium hexametaphosphate solution, wet sieved (>63 μm), rinsed with distilled water, and oven-dried at 30°C overnight. Approximately 30 *T. sacculifer* shells were picked from the 250–355 μm size fraction of each sample. This species was selected because it provided the most continuous stratigraphic record relative to all other mixed-layer dwelling foraminiferal species and is an accurate recorder of paleo-SSTs (Hastings et al., 1998; Wycech, 2017). Both glassy and frosty foraminifers were present in the samples with the former indicating exceptional preservation (Pearson et al., 2001, 2007; Sexton et al., 2006; Wycech et al., 2016). Only well-preserved, ideally glassy *T. sacculifer* shells were selected for analysis (see Table S1 for shell preservation notes).

The Mg/Ca ratios of the shells were measured by a Thermo Finnigan Element2 sector-field inductively coupled plasma mass spectrometer at the University of Colorado-Boulder (Marchitto, 2006). The shells were gently crushed between two glass slides and cleaned by the clay-removal, oxidative, and reductive procedure outlined in Boyle and Keigwin (1985) and modified by Boyle and Rosenthal (1996). Long-term analytical precision is ±0.5%, or ∼0.02 mmol/mol (1σ), based on measurement of a 1.65 ± 0.01 mmol/mol liquid Mg/Ca consistency standard. Replicate analyses (on splits of the crushed shell sample) were performed on over 20% of the samples with standard deviations on Mg/Ca ratios that ranged from 0 to 0.47 mmol/mol (pooled sd = 0.14 mmol/mol, n = 41 samples) for Site 625 and 0–1.14 mmol/mol (pooled sd = 0.30 mmol/mol, n = 31 samples) for Site 997.

SSTs were calculated using the *T. sacculifer* calibration of Anand et al. (2003). This Mg/Ca-temperature calibration utilized sediment trap shells also from the Atlantic and has been shown to accurately reconstruct SSTs from the Mg/Ca ratios of fossil *T. sacculifer* shells (Wycech, 2017). We have modified the calibration from Anand et al. (2003) following the method used by Medina-Elizalde et al. (2008) to correct for the lower Mg/Ca ratios of Pliocene seawater (Mg/Ca_{sw}),

$$Mg/Ca = B\left(\frac{Mg/Ca_{sw}}{5.17}\right)e^{AT} \quad (1)$$

where *Mg/Ca* is the measured ratio in fossil shells (mmol/mol), B is 0.347, Mg/Ca_{sw} is the time-dependent seawater ratio from Zeebe and Tyrrell (2019), 5.17 is modern Mg/Ca_{sw} (mol/mol; Rausch et al., 2012), A is 0.09, and T is temperature (°C). Compared to the SSTs calculated with the published calibration, the Mg/Ca_{sw} adjustment increases SSTs by 0.5°C on average with the smallest difference for the youngest samples (<0.1°C) and the largest difference ∼5 Ma (2.5°C). This approach neglects secondary influences from salinity and pH (Gray & Evans, 2019) for which we have no useful constraints.

2.2. Pliocene SST Reconstruction Via Principal Component Analysis

The enlisted principal component analysis (PCA) method relies upon the relationship between the contemporary mean annual SSTs in the full field (gridded map, Figure 2b) and a limited field that samples only paleo-proxy locations (spatial points, Figure 2c) to reconstruct the full field paleo-SST from only the limited field paleo-SST data set.

2.2.1. Contemporary Data

Monthly anomalies of SSTs gridded at 2° × 2° over the Atlantic region from 2°S to 60°N and from 96°W to 26°E, from 1854 to 2018 are from the NOAA National Climatic Data Center (NCDC) Extended Reconstruction Sea Surface Temperature (ERSST) version 3b data set (Smith et al., 2008). Grid points within the Pacific Ocean were removed to isolate variability within only the Atlantic. We calculated monthly SST anomalies from the 1981–2010 climatology and averaged from May to the following April to obtain annual averages. The May—April period was chosen to capture a complete Boreal winter season when the ocean-atmosphere interaction occurs most strongly in the basin. The widely used SST-based index in the North Atlantic, AMO, is also computed from the historical SST anomalies as averages over the specific region 2°S to 60°N and 0°E to 80°W (Enfield et al., 1999;

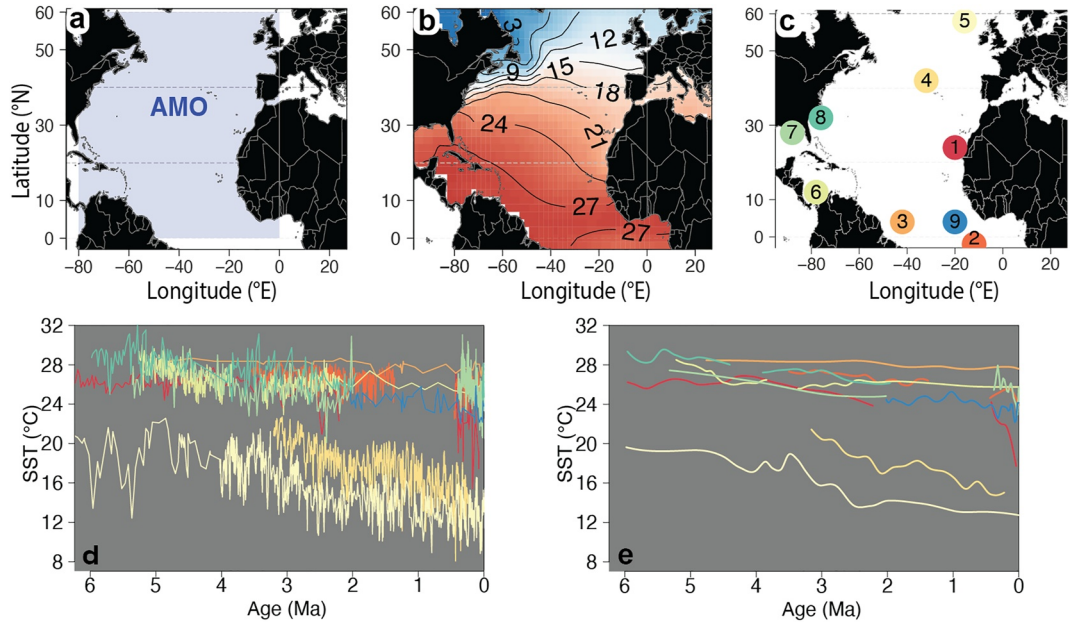

Figure 2. Maps of the North Atlantic showing (a) Atlantic multidecadal oscillation index region (see Section 2.2.1 for coordinates), (b) mean sea-surface temperatures (SSTs) (°C) of the contemporary full field (1854–2018), and (c) the limited field site locations (Table 1). (d) Plio-Pleistocene SST records. (e) Plio-Pleistocene SST records smoothed using a second order local polynomial (local neighborhood = 20% nearest data points).

Green et al., 2017; Trenberth & Shea, 2005). This provides a quantitative means to monitor the state of AMO and to provide a proxy for trans-equatorial heat transport in the Atlantic, and consequently the variability of the inter-tropical convergence zone (ITCZ) and its impact on the adjoining continental rainfall.

2.2.2. Paleo SST Data

The new SST records described in Section 2.1 were added to a compilation of Pliocene SST records from two proxies: Mg/Ca (2 other sites) and $U^{k'}_{37}$ (5 sites) (Table 1). The $U^{k'}_{37}$ proxy is derived from organic molecules called alkenones produced by some species of marine phytoplankton known as coccolithophores. The degree of unsaturation (number of double bonds connecting carbon atoms) in the alkenones record the temperature of the water in which the coccolithophore live. The Unsaturation Index is specifically defined by the ratio between the diunsaturated ($C_{37:2}$) alkenones to the sum of triunsaturated ($C_{37:3}$) and diunsaturated alkenones, $U^{k'}_{37} = C_{37:2}/(C_{37:3} + C_{37:2})$ (Brassell et al., 1986; Marlowe et al., 1984; Volkman et al., 1980).

Although Pliocene SST records from 40 sites in the North Atlantic have been published, we use only the $U^{k'}_{37}$- and Mg/Ca-based records from 9 sites that have Plio-Pleistocene temporal coverage (5 to <0.5 Ma; Figure 2, Tables 1 and Table S1). The selected records also have numerous samples that are less than or equal to 0.5 Ma in age in order to effectively calculate the average SST from 0 to 0.5 Ma that is used as reference to define the Pliocene SST anomalies. This approach reduces the probability of aliasing because the youngest sample at each site was not necessarily contemporaneous with sites from the other study. So, calculation of anomalies from only the core top samples could lead to bias in the PCA reconstruction. The defined "base period" (0–0.5 Ma) includes multiple data points from each record (between 54 and 1,229, and 568 on average). As multiple glacial-interglacial cycles are included in this base period, the interval from 0 to 0.5 Ma has a cold bias. Accordingly, reconstructed SSTs compared to the base period rather than the modern, instrumental period or the Holocene, share this cold bias. The new Mg/Ca-based SST records described in Section 2.1 were combined with previously published Pleistocene SST records at the same or nearby sites (Carlson et al., 2008; Ziegler et al., 2008, Table 1) to establish base period conditions in these grid cells.

Published SST records were previously calculated with various calibrations. For consistency, we recalculated SSTs from $U^{k'}_{37}$ and Mg/Ca ratios using one calibration per proxy. Raw $U^{k'}_{37}$ values were converted to SST using the global calibration of Müller et al. (1998), and we explored the effect of using Tierney and Tingley's (2018)

Table 1
Atlantic Sea-Surface Temperature (SST) Proxy Records

Site	Core	Latitude (°N)	Longitude (°E)	Water depth (m)	Species	Youngest age (Ma)	Oldest age (Ma)	Hiatus (Ma)[a]	Average sampling resolution (ka)[b]	References
$U^{k'}_{37}$ Records										
1	ODP 958	23.999	339.999	3,728	NA	2.21	6.47	0.43–2.21	36	Herbert and Schuffert (1998)
					NA	0.08	0.43		12	Pflaumann et al. (1998)
2	ODP 662	−1.390	348.261	3,728	NA	0.001	3.54	0.46–1.37	2	Herbert et al. (2010)
3	ODP 925	4.204	317.511	1,713	NA	0.02	38.49	4.78–7.15	430	Zhang et al. (2013)
4	DSDP 607	41.001	327.043	3,042	NA	0.25	3.20	NA	4	Lawrence et al. (2010)
5	ODP 982	57.517	344.133	1,134	NA	<0.01	16.00	NA	13	Herbert et al. (2016), Lawrence et al. (2009)
Foraminifer Mg/Ca records										
6	ODP 999[c]	12.744	281.261	2,828	*T. sacculifer*	<0.01	4.34	NA	11.4	O'Brien et al. (2014)
					T. sacculifer	2.01	5.26			Groeneveld (2005)
7	ODP 625	28.832	272.840	900	*G. ruber*	0.001	0.40	0.40–2.001	0.6	Ziegler et al. (2008)
					T. sacculifer	2.001[d]	5.36		21	This study
8	KNR140-51GGC	32.783	283.717	1,790	*G. ruber*	0.008	0.03	0.03–1.95, 3.91–4.42	0.5	Carlson et al. (2008)
	ODP 997	31.843	284.532	2,770	*T. sacculifer*	1.95[d]	5.98		27	This study
9	ODP 668	4.77	339.073	2,694	*G. ruber*	0.004	2.05	NA	39	Hönisch et al. (2009)

[a]Defined as the years (not duration) of the temporal gap in the records if present. [b]Excludes temporal gaps at Sites 1–3, 7, and 8. [c]Records were combined to produce one record with no hiatus. [d]Study also analyzed one Holocene (<0.01 ka) sample.

BAYSPLINE instead (Sections 4.4 and S1). Mg/Ca-based SSTs were recalculated using the calibration and Mg/Ca_{sw} correction detailed in Section 2.1. However, the pre-exponential constant (B) in Equation 1 was set to 0.395 for the records that report Mg/Ca ratios of a different foraminifer species (*Globigerinoides ruber*; see Table 1). Post-depositional dissolution (Regenberg et al., 2014) was assumed to be minor since all Mg/Ca sites lie above 3 km water depth in the North Atlantic.

The temporal resolution of the selected records ranges from 500 to 430,000 years (average = 49,708 years). Smoothing of the raw SST records (Figures 2d and 2e) prior to PCA resolve issues related to inter-site differences in sampling resolution and allows for the PCA to be completed using SSTs from all sites at any time point within the study interval. Records were smoothed using a local polynomial of 20% nearest neighbors, which captures a conservative representation of each SST record and is not of a sufficient resolution to assess effects of orbital variations on the reconstruction. The smoothing was not performed over temporal gaps (hiatuses) that lasted longer than 0.4 Ma years (see Table 1 and discontinuous records in Figures 2d and 2e). Records with these gaps were excluded from the reconstruction during these intervals. Spatially, both the Mg/Ca and $U^{k'}_{37}$ records cover a large (~60°) latitude range, but all three sites from the Gulf of Mexico and northwest Atlantic are derived from Mg/Ca ratios.

3. Reconstruction Methodology and Assessment

We adapted the reduced-space method (Figure S1 in Supporting Information S1) based on PCA proposed by Gill et al. (2016) for Holocene SST reconstruction in the tropical Pacific and subsequently used for Holocene-monsoon reconstruction (Gill et al., 2017) and Pliocene-SST reconstructions in tropical Pacific (Wycech et al., 2020). We review the technique in context to this study and refer the reader to the papers cited above for details.

3.1. Principal Component Analysis

PCA decomposes space-time multi-variate data into orthogonal space-time components, also known as modes, via eigen decomposition of the covariance matrix (Von Storch & Zwiers, 2001). The spatial components or the eigenvectors, also known as Empirical Orthogonal Functions (EOFs), capture spatial variability and the Principal Components (PCs) contain the temporal variability. Multiplying the PCs by the eigenvectors reproduces the original data space and multiplying the original data by the eigenvectors produces the PCs. This property of being able to transform between the data and PC space, preserving the total data variance, while maintaining the orthogonality of the PCs and EOFs, makes this technique attractive for analysis of large space-time climate data. The order of the PCs reflect the percentage of total variance resolved (i.e., the first few PCs capture the majority of the variance).

First, we completed a PCA on the full field of contemporary SSTs in the Atlantic study area (60°N–2°S, 26°E−96°W) using the complete historical SST record (1854–2018). The eigenvalue (λ) spectrum (Figure 3a) was utilized to define the number of PCs included in the reconstruction as eigenvalues for PCs 1–4 are above the noise floor ($\lambda > 0.05$) and together explain 68% of the total variance in the historical SST record. This allowed for the statistical model to maximize the total variance while minimizing noise.

Next, we completed a PCA on the limited field of contemporary SSTs, that is, the SST field sampled only by the spatial points with paleo-SST records. The first five modes were retained as they together explain 90% of the limited field's total variance (Figure 3a). Each of the four PCs from the full field PCA are linearly regressed against the five PCs from the limited field PCA resulting in four linear regression models, one for each mode. For each time point, say 3 Ma, the contemporary limited field eigenvector matrix is multiplied by the paleo-SST anomaly at each of the limited field locations to obtain the paleo PCs of the limited field. Estimates of the four PCs of the corresponding full field are obtained from the fitted linear regression models. Thus, the four PCs of the full field are converted to the SST-anomaly space via multiplication with the contemporary full field eigenvectors to reconstruct the paleo-SST anomalies for the full field at 3 Ma. This is repeated for any desired time point—both in the observational and paleo periods. In addition to the reconstructions at distinct time points (2, 3, 4, and 5 Ma), reconstructions were performed at smaller (0.02 Ma) time-steps from 5 to 1 Ma to generate a time series for the AMO-like index for a more comprehensive view of Plio-Pleistocene changes in North Atlantic SSTs.

To quantify the uncertainty in the reconstructions, we generated 500 ensembles of the full field PC estimates based on the PC standard errors from the regression models, which are normally distributed with mean zero and a variance estimated from the regression model. Error deviations are randomly generated from the corresponding normal distributions of the errors, which are added to the mean estimate from the regression, to obtain ensembles. Ensembles for the first three PCs generated from the linear regression. Ensembles for each of the remaining PCs generated by bootstrapping values from the original PCs at each grid point. The SST anomaly ensembles provide nominal uncertainty estimates. While useful, this approach typically underestimates the full standard error because it does not include the uncertainties in the data or regression model parameters. Future studies should look to Bayesian regression methods, which incorporate all sources of error and thereby provide robust estimates of uncertainty (see Gelman & Hill, 2006).

3.1.1. PCA Patterns

We show the spatial and temporal patterns of the three leading PCs in Figure 3—as they individually capture the majority of the variance. Spatially, the leading three limited field PCs are plotted as filled circles and compared with the corresponding PCs from the full field analysis using the same color scheme (Figures 3b–3d). Measured and reconstructed time series of the corresponding PCs are shown below each panel. It can be seen that in each plot the two correlate on both decadal and annual time scales.

The first mode shows a warming trend over time as well as warming throughout the North Atlantic (Figure 3b). This warming pattern in the Atlantic is consistent with other studies over the past century (Chen & Tung, 2018). The second mode (Figure 3c) exhibits spatial and temporal trends reminiscent of AMO, that is, warmer and cooler SSTs on opposite sides of the equator and multi-decadal SST oscillation (Enfield et al., 2001). The third mode captures interannual variability with a spatial warm-cool-warm pattern across the North Atlantic (Figure 3d). This classic tripole pattern in the North Atlantic with warm SSTs in the high and low latitudes and cold SSTs in the midlatitudes (~40°N) has been related to air-sea interaction driven by North Atlantic Oscillation (e.g., Deser et al., 2010; Marshall et al., 2001).

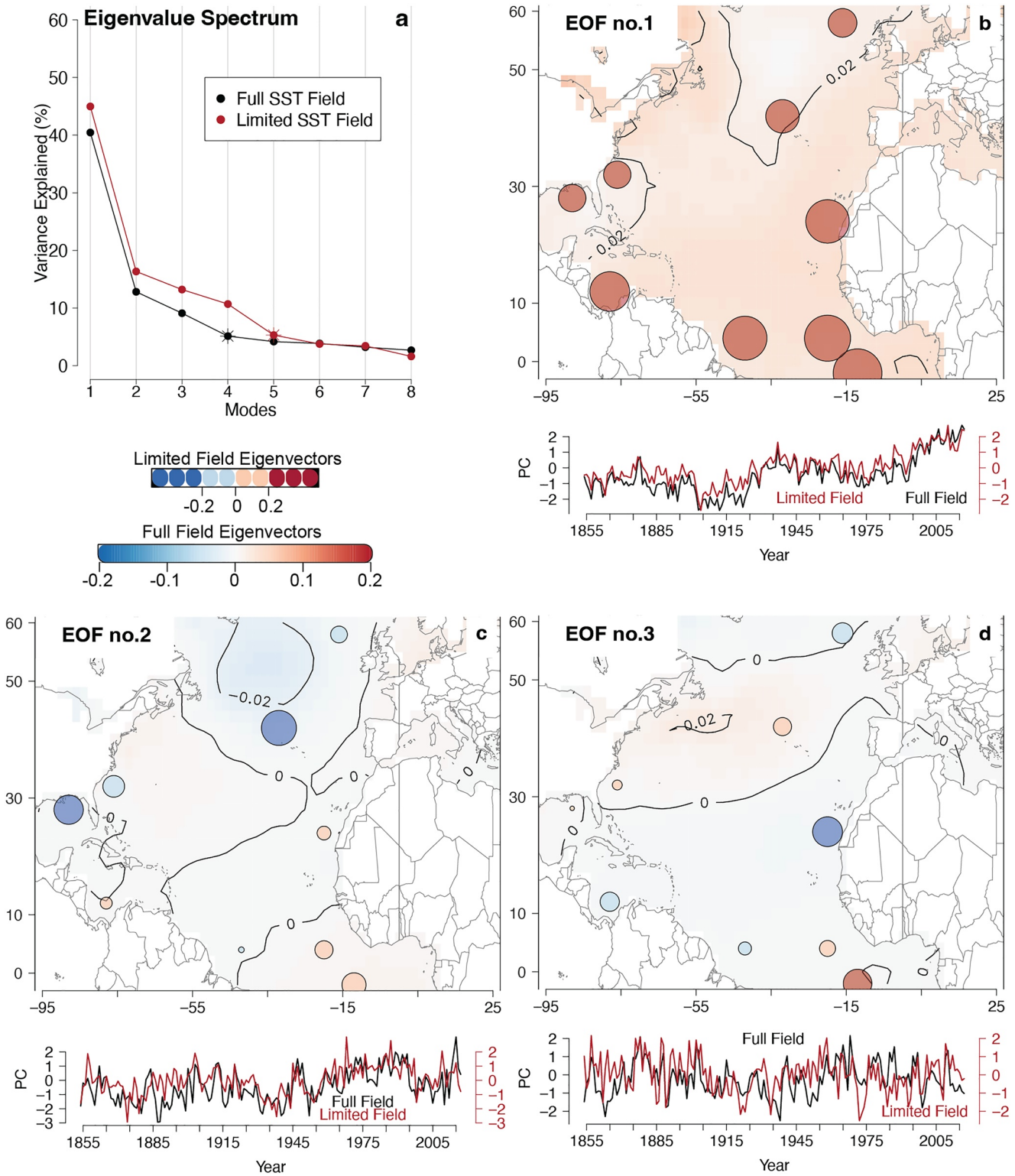

Figure 3. (a) Eigenvalue spectra for the limited sea-surface temperature (SST) field (red) and the full SST field (black). Asterisks mark the points just above the noise floor (5%). The first four eigenvalues are $\lambda_1 = 0.405$, $\lambda_2 = 0.128$, $\lambda_3 = 0.091$, and $\lambda_4 = 0.051$ for the full field and the first five eigenvalues are $\lambda_1^{\dagger} = 0.450$ and $\lambda_2^{\dagger} = 0.163$, $\lambda_3^{\dagger} = 0.132$, $\lambda_4^{\dagger} = 0.107$, and $\lambda_5^{\dagger} = 0.053$ for the limited field. (b–d). Full field Empirical Orthogonal Functions (EOFs) (shaded map) and normalized Principal Components (PCs) (black time series) of the three leading modes of the principal component analysis. Limited field EOFs (circle size represents EOF magnitude and color shows the sign) and normalized PCs (red time series). All EOFs are multiplied by their respective eigenvalues to show relative magnitudes through subsequent modes.

Overall, agreement between the spatiotemporal trends of the limited and full field eigenvectors (Figures 3b–3d) indicates the limited field is a good representation of the region and bodes well for paleo reconstruction from the selected SST records (Table 1). It is useful to note that the spatial distribution of the eigenvector magnitude is heterogeneous across the region with a distinct pattern only for EOF1 where weightings are highest in the low latitudes (Figures 3b–3d).

3.1.2. Assumptions for Applications to Paleoclimate Reconstructions

The assumptions noted in Wycech et al. (2020) concerning the application of the limited field approach to Pliocene reconstructions apply to this study as well. In short, we assume a linear relationship between the limited and full field contemporary SSTs, that the temperature-proxy relationships observed in modern sediments or in laboratory culture are applicable back to 5 Ma, and that the biology of the organisms carrying the paleotemperature proxies did not change between the Pliocene and today. We also assume that the spatiotemporal variations in the contemporary SST record and the associated teleconnections, which produce rainfall in the Sahel, apply as far back as 5 Ma. The last assumption is an acceptable one given evidence for warm North Atlantic Pliocene SSTs (Dowsett, 2007; Dowsett et al., 1992, 1996; Robinson et al., 2008) and the fact that modern teleconnections associated with a warm phase of AMO are also evident among global Pliocene climate records (Brunet et al., 1995; Louchart et al., 2004; Vignaud et al., 2002). We also assume that the proxies record annual average SSTs throughout the Atlantic, which carries risk because some of our study sites experience high seasonality and the biological carriers of the proxies can sometimes prefer variable water depths or specific seasons (Harada et al., 2001; Leduc et al., 2010; Müller & Fischer, 2001; Ohkouchi et al., 1999; Rae et al., 2014). For example, the average water depth habitat for *T. sacculifer* and *G. ruber* in the subtropical North Atlantic is estimated to be 30–60 m (Rebotim et al., 2017; Wycech, 2017). The modern difference in temperature between 50 and 0 m ranges from 0°C to 4°C at our study sites (Locarnini et al., 2010; Figure S5 in Supporting Information S1) with the largest temperature differences occurring in areas of upwelling where *T. sacculifer* and *G. ruber* prefer water depths of less than 30 m (Ravelo & Andreasen, 1999). Our Pliocene reconstructions therefore reflect SSTs within errors of the proxies and may in fact be conservative underestimates. Additionally, we acknowledge that the SST reconstructions reflect the mean state of the North Atlantic due to the time-averaging over glacial-interglacial cycles given the slow deposition of deep-sea samples and the smoothing of the SST records. Our results therefore do not elucidate interdecadal variability, a key component of the modern AMO phenomenon. Although it is impossible to resolve the frequency or amplitude of Pliocene AMO, an AMO-like SST pattern observed for the Pliocene can still prove informative considering the teleconnections associated with modern AMO.

3.1.3. The AMO Paradigm and Its Validity for Pliocene Reconstruction

The observation and definition of AMO by Enfield et al. (2001) is apparent in contemporary records but requires a different interpretation when applying it to paleoclimate reconstructions. The temporal resolution of the reconstructions presented herein, even at the finest scale (2 kyr), cannot capture the "multidecadal" aspects of AMO. Rather, the Pliocene reconstruction is intended to assess mean SSTs over the region in which modern AMO is observed and utilize our knowledge of modern AMO teleconnections to reconstruct Sahel rainfall in the Pliocene. The definition of AMO has since been redefined as Atlantic Multidecadal Variability (AMV) because the phenomenon may in fact be related to multiple low-frequency signals rather than a single frequency oscillation (e.g., Sutton et al., 2018; Zhang, 2017). Given the goals of this study, either term would be appropriate, so we retain the use of AMO as it was the first defined.

3.2. PCA Calibration and Validation

We use β and R^2 statistics to evaluate the ability of the PCA to reconstruct the contemporary full-field SSTs from the limited-field. The resolved variance statistic (β) is defined as

$$\beta = 1 - \frac{\sum(y - \hat{y})^2}{\sum y^2} \tag{2}$$

where y is the contemporary data and $\hat{y}$ is the reconstructed data for the full period (1854–2017). A β statistic of 1 indicates a perfect fit while negative values indicate two random series. The β statistic is calculated for each $2° \times 2°$ grid point within the Atlantic domain and range from 0.1 to 0.9 (Figure 4a). The lowest β values occur in the western North Atlantic around the Gulf Stream, both where there are no/few limited-field sites and where the

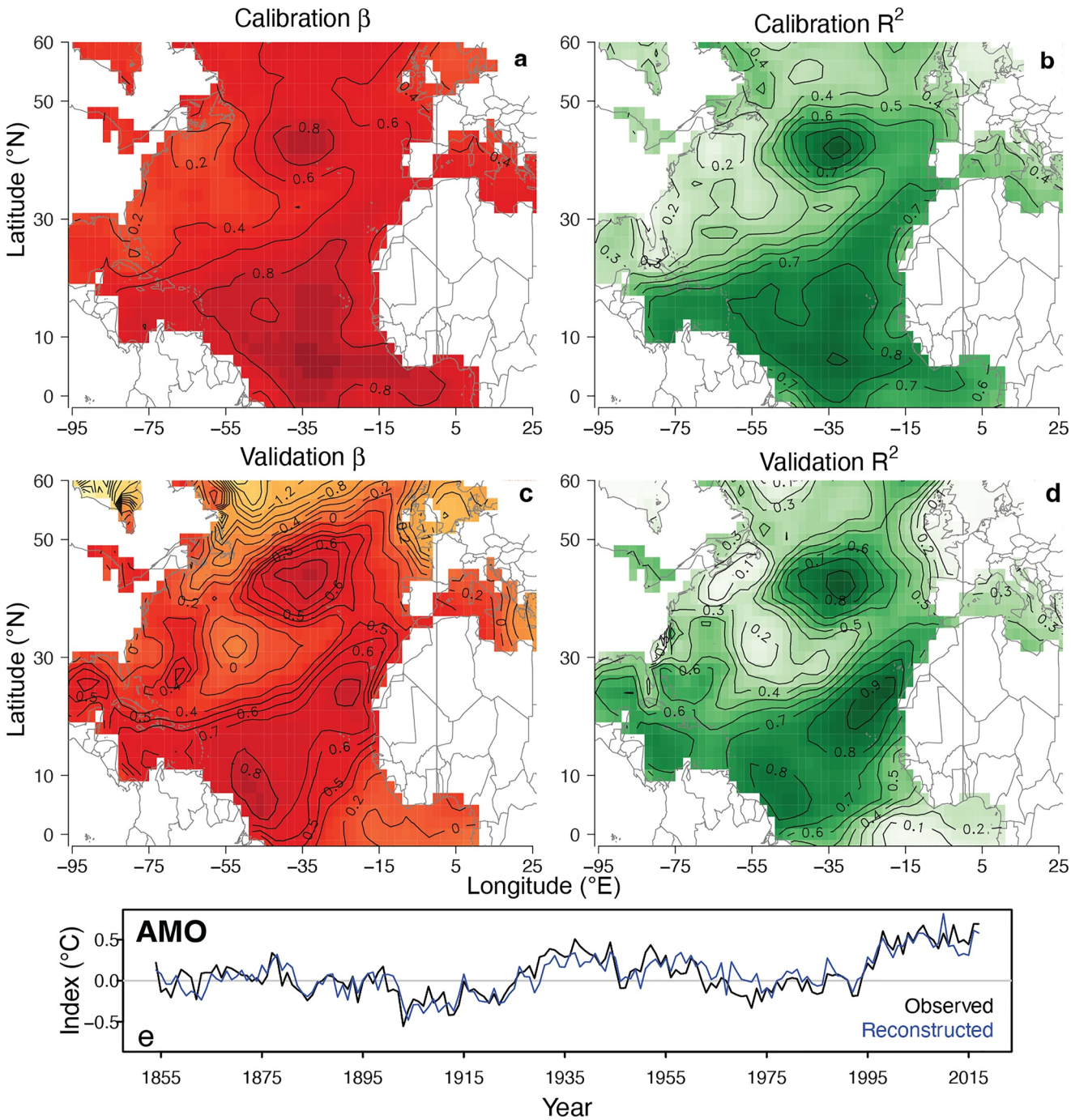

Figure 4. Calibration and validation of the principal component analysis (PCA) model. The β statistic represents the resolved variance captured by the reconstructed contemporary data. The R^2 represents the strength of correlation between the reconstructed and observed contemporary data. The β maps and R^2 values were plotted with the same scale bar for both calibration and validation. (a, b) Calibration statistics for the sea-surface temperature (SST) PCA model (shading and black contours) showing the model's skill to reconstruct the contemporary data set. (c, d) Validation entailed training the model on 1980–2013 data and using output parameters to estimate SSTs from 1900 to 1979. (e) Model-data comparison of historical time series of the reconstructed (blue line) and observed (black line) Atlantic multidecadal oscillation index.

loadings of the leading EOF are small (Figure 3b). Conversely, the highest β values (up to 0.9) occur in the central North Atlantic and in the tropical and eastern subtropical North Atlantic where there are numerous limited-field sites and the loadings of the first EOF are high. The squared correlation statistic (R^2) provides the strength of correlation between the reconstructed and observed SSTs at each grid point (Figure 4b). This is consistent with

the β map, as expected—regions with higher values of β correspond to higher values of R^2 and vice-versa. As with the map of β the regions with few limited-field sites, the western Atlantic, has lower R^2 values (0.2–0.4) than the region with abundant limited-field sites, the central, tropical and eastern subtropical North Atlantic (R^2 = 0.6–0.9).

To validate the statistical model, we trained the reconstruction PCA using the recent SSTs (1980–2013) which are of higher fidelity, reconstructed the full-field SSTs for an earlier contemporary period (1900–1979), and computed the β and R^2 statistics to assess the fitting and correlation, respectively, between the observed and reconstructed SSTs (1900–1979). The interval 1900–1979 was selected for validation to remove the abrupt warming SST trend for 1854–1899 and thereby ensure the PCA was validated for a time interval that had comparable variability to the interval upon which it was trained. The β results of the validation experiment (Figure 4c) range from ~−3.4 to 0.9 with the largest positive and most negative β values are found in the same regions large and small values of β in Figure 4a. The validation R^2 values (Figure 4d) range from <0.01 to 0.9 and have a spatial pattern that is similar to the β values.

Both the calibration and validation statistics indicate regions where the reconstruction is most and least reliable, primarily a function of the spatial distribution of limited field sites and the loadings of the leading EOFs. The β values for both the calibration and validation of the PCA (Figures 4a and 4c) are typically positive in the North Atlantic, which bolsters confidence in our PCA approach to reconstructing Pliocene SST patterns in this target region. However, additional paleo proxy data from data-sparse regions will help to capture the variability more robustly. Since a main objective is to reconstruct the average SST anomaly over the North Atlantic, we further validated the PCA by reconstructing a time series of contemporary SSTs using the method described in Section 3.1. SSTs were reconstructed for each year of the contemporary period, and the "reconstructed" AMO index was computed and compared with the AMO index from the "observed" historic SSTs (Figure 4e). The reconstructed and historic AMO indices are highly correlated (Spearman's rho = 0.88) and are within 0.1°C of one another on average. The ability to reconstruct the AMO index with a relatively small number of grid point SSTs (limited field) is noteworthy. The reconstructed values of AMO are slightly smaller than historic values in that some of the highest absolute values are underestimated. The latter point is important because it indicates that the limited-field component yields a conservative estimate of AMO intensity. In this comparison of reconstructed and observed AMO, the PCA is capturing multidecadal variability since all input data is contemporary. For the Pliocene, however, the reconstructed AMO-like index is simply the average SSTs over the AMO region and does not capture actual multidecadal oscillation of the SSTs.

4. Results—Pliocene Reconstructions

4.1. New Plio-Pleistocene SST Records From the Northwest Atlantic

We have reconstructed Plio-Pleistocene SSTs at ODP Sites 625 in the Gulf of Mexico and ODP Site 997 on the Blake Ridge to provide insight into a relatively understudied region for this time period. Each Pliocene SST record is compared to the modern SST (January–December average SST from 1981 to 2010, Smith et al., 2008) at the site. From 6 to 2 Ma, both records indicate SSTs were on average warmest in the early Pliocene (~5 Ma) and started to cool at ~4.5 Ma. Specifically, at sites 625 and 997 the average SSTs prior to 3.6 Ma were respectively 1.8°C and 1.6°C warmer than those for 3.6–2 Ma. The warmth at Site 625 was briefer than at Site 997 as SSTs at the former approached modern conditions by ~3.9 Ma. In contrast, SSTs at Site 997 were on average 3°C warmer than modern from 6 to 2 Ma.

Reconstructed Plio-Pleistocene SSTs are compared to Late Pleistocene-Holocene SSTs recalculated from previously published Mg/Ca ratios of the mixed-layer dwelling foraminifer *G. ruber* (Carlson et al., 2008; Ziegler et al., 2008; Figures 1b and 1c). Note that the most recent sample (~0 Ma) at each site were analyzed for this study and are based on the Mg/Ca ratios of *T. sacculifer*. The late Pleistocene-Holocene SSTs at Site 625 show similar average values as in the early Pleistocene, and the average SST for 0.4–0 Ma is within 0.1°C of the modern value (25.3°C, 1981–2010 mean). At Blake Ridge, the SSTs for 25–0 ka are on average 1.2°C warmer than the modern SST (24.7°C, 1981–2010 mean), but the core top (0–2 cm depth) is within 0.1°C of modern. The facts that late Pleistocene-Holocene records both are similar to the modern SST and are consistent with the trends observed in the Plio-Pleistocene intervals bolster confidence in our SST reconstruction method.

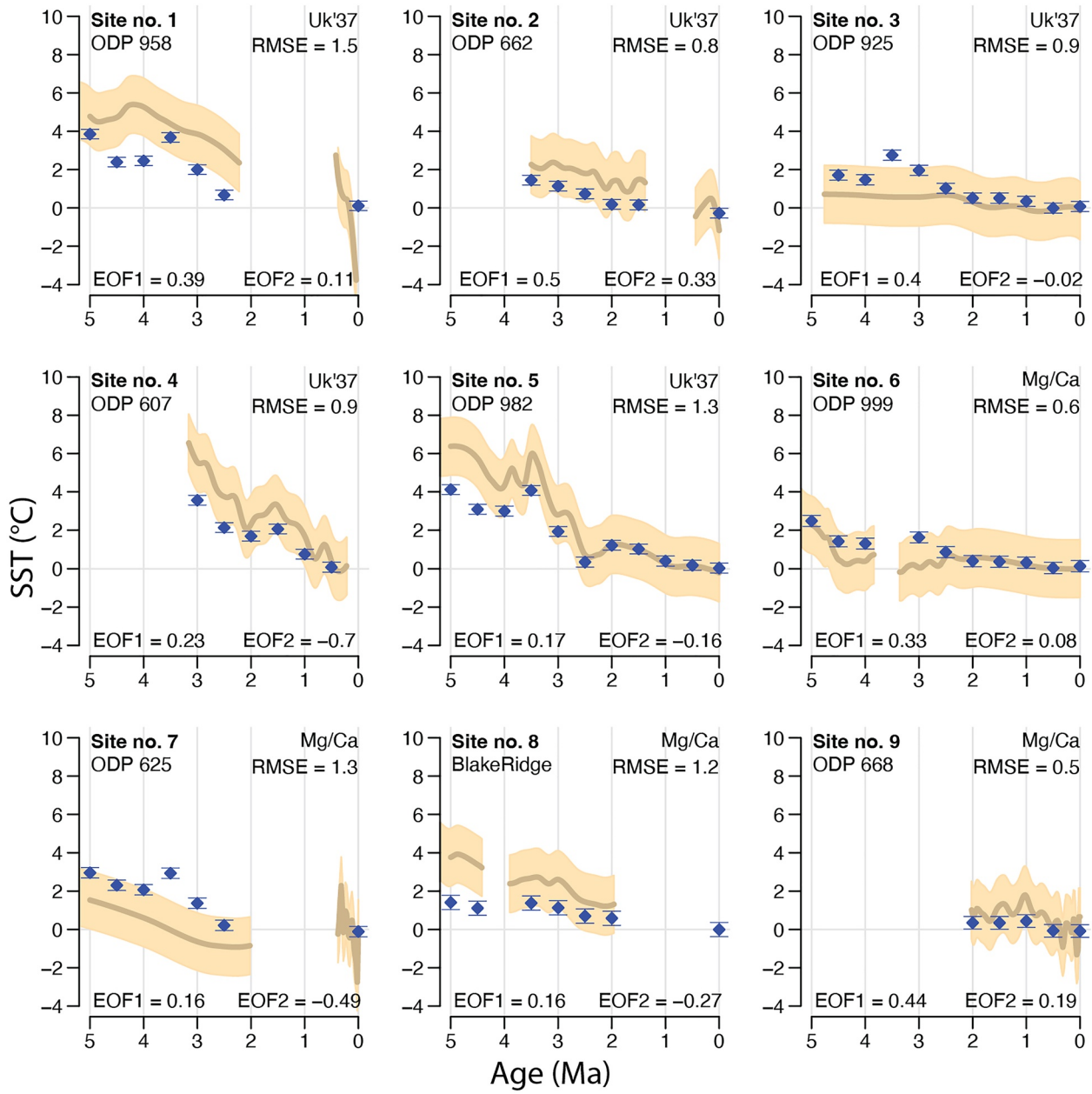

Figure 5. Scatterplots of the individual sea-surface temperature (SST) proxy records (yellow) from the Atlantic with the reconstructed SST values for the spatial grid point closest to each record (blue). Standard errors of the proxy-based SSTs are in light yellow around each record: ±1.2°C for Mg/Ca (Anand et al., 2003; Dekens et al., 2002) and ±1.5°C for $U^{k'}_{37}$ (Müller et al., 1998). Standard errors on the reconstructed SSTs are shown as blue whiskers. Site numbers (upper left) match those in Figure 2 and Table 1. The root mean square error (RMSE) quantifies how closely the proxy-based SSTs match those reconstructed by the model. The first two eigenvector values (EOF1 and EOF2) are noted at each location.

4.2. Limited Field SST Reconstruction

In order to assess how well the method reconstructs each paleo-SST record, we determined the goodness of fit between the smoothed paleo-SSTs and the reconstructions from our method using the root mean square error (RMSE) (Figure 5). The reconstructions were performed at 0.5 Ma intervals from 5 to 0 Ma except for intervals where the proxy-based SST record was not present. The first two eigenvector values are noted for each site and indicate the relative contribution of these data to the full field reconstruction. The magnitude and sign (positive or negative) of these eigenvectors respectively correspond to the area and color of the circles mapped in Figures 3b and 3c. The RMSE values are typically within the standard errors of the SST reconstruction (1.2°C for Mg/Ca,

1.5°C for $U^{k'}_{37}$). At the sites where the RMSE is largest (e.g., sites 1, 5, and 7), the largest mismatch between the original proxy-based SST records and those reconstructed by the PCA occurs in the earliest Pliocene interval (5–3 Ma). There may be site-specific explanations for the disagreement such as temporal differences in rates of upwelling or deep-water formation or marked differences between Pliocene and present-day SSTs not captured by variability over the past 164 years. Overall, however, the PCA reproduces the SSTs regardless of the proxy type, and none of the proxies consistently bias SSTs in one direction. These observations indicate that the selected temperature calibrations are appropriate at our study sites.

4.3. North Atlantic SST Reconstruction

The SST reconstruction was first completed for the base period (0–0.5 Ma), which entailed averaging the SSTs reconstructed at 20 ka intervals through the base-period interval (Figure 6a). Absolute SSTs were then reconstructed (Figures 6b–6e) for 5, 4, 3, and 2 Ma. The reconstruction of absolute SSTs provide a comparison relatable to modern and base-period conditions as well as lower SST boundary conditions for ocean and/or atmospheric climate models in future studies.

In comparison to absolute SST maps, a more useful means to reconstruct SSTs is to calculate SST differences (i.e., anomalies) between a Plio-Pleistocene time period and the base period (Figure 6a). Maps of SST anomalies calculated in this manner for 5, 4, 3, and 2 Ma are shown in Figures 6g–6j. These snapshots are accompanied by a time-series of the AMO-like index generated by PCA analysis at 0.02 Ma time steps from 5 to 1 Ma (Figure 6f). Note that abrupt changes in the time series result from discontinuities in limited field SST records used in the reconstruction—they do not reflect abrupt changes in the index and all occur within the standard error of the previous baseline values.

Overall, the Plio-Pleistocene North Atlantic was characterized by warm SSTs with average anomalies of 3.5°C during the warmest interval (~5 Ma) (Figure 6j). At peak, SST anomalies exceeding 5°C are present in the Labrador Sea and northernmost Atlantic (Figure 6j). The Pliocene results showing warm SST anomalies in the North Atlantic (Figures 6g–6j), and a positive AMO-like index throughout the study interval (Figure 6f) indicate that mean conditions during this time period resembled the modern warm phase of AMO (Chen & Tung, 2018; Enfield et al., 1999).

The standard errors on the reconstructed SST anomalies at 2, 3, 4, and 5 Ma range from 0.2°C to 1°C with the largest errors occurring in regions either with few limited field sites (e.g., the northwest Atlantic and Labrador Sea) and/or with highly variable SSTs (Figures 6k–6n). Although the largest errors in the reconstruction occur in the regions with the largest positive SST anomalies, the warm anomalies exceed standard errors of the reconstruction by several times.

4.4. Calibration Sensitivity to PCA Reconstruction

Two sensitivity analyses was performed to assess if and how the reconstruction changed when other SST calibrations were applied. First, $U^{k'}_{37}$-based SSTs were calculated using the Bayesian spline regression model (BAYSPLINE; Tierney & Tingley, 2018) rather than the Müller et al. (1998) calibration. Temperatures reconstructed using BAYSPLINE do not have an upper limit, but the uncertainties at the warm end ($U^{k'}_{37} > 0.8$) are large (~4.4°C at 29.4°C). Although $U^{k'}_{37}$ values at many of the study sites are high (~1), the full field SST reconstruction using BAYSPLINE with a prior standard deviation of 10°C is no more than 1.0°C higher than that derived from the Müller et al. (1998) calibration (Figure S2 in Supporting Information S1). Regional SSTs vary depending upon which $U^{k'}_{37}$ calibration is applied. The study area is, however, large so the two reconstructions produce average SST anomalies over the AMO region that only differ by 0.4°C (Figure S4 in Supporting Information S1). Thus, the $U^{k'}_{37}$-based SSTs derived from these two calibrations are not distinguishable from one another considering the errors in each.

Second, Mg/Ca-based SSTs were calculated using the Evans et al. (2016) calibration which accounts for the non-linear effects of both temperature and Mg/Ca_{sw} on foraminifer Mg/Ca ratios (Figure S3 in Supporting Information S1). The sensitivity analysis used the same Mg/Ca_{sw} estimates as that of the original reconstruction (Zeebe & Tyrrell, 2019). Since the Evans et al. (2016) calibration is derived from *G. ruber*, all *T. sacculifer*-based Mg/Ca ratios were increased by 10.3% to compensate for the inter-species difference in the pre-exponential constant

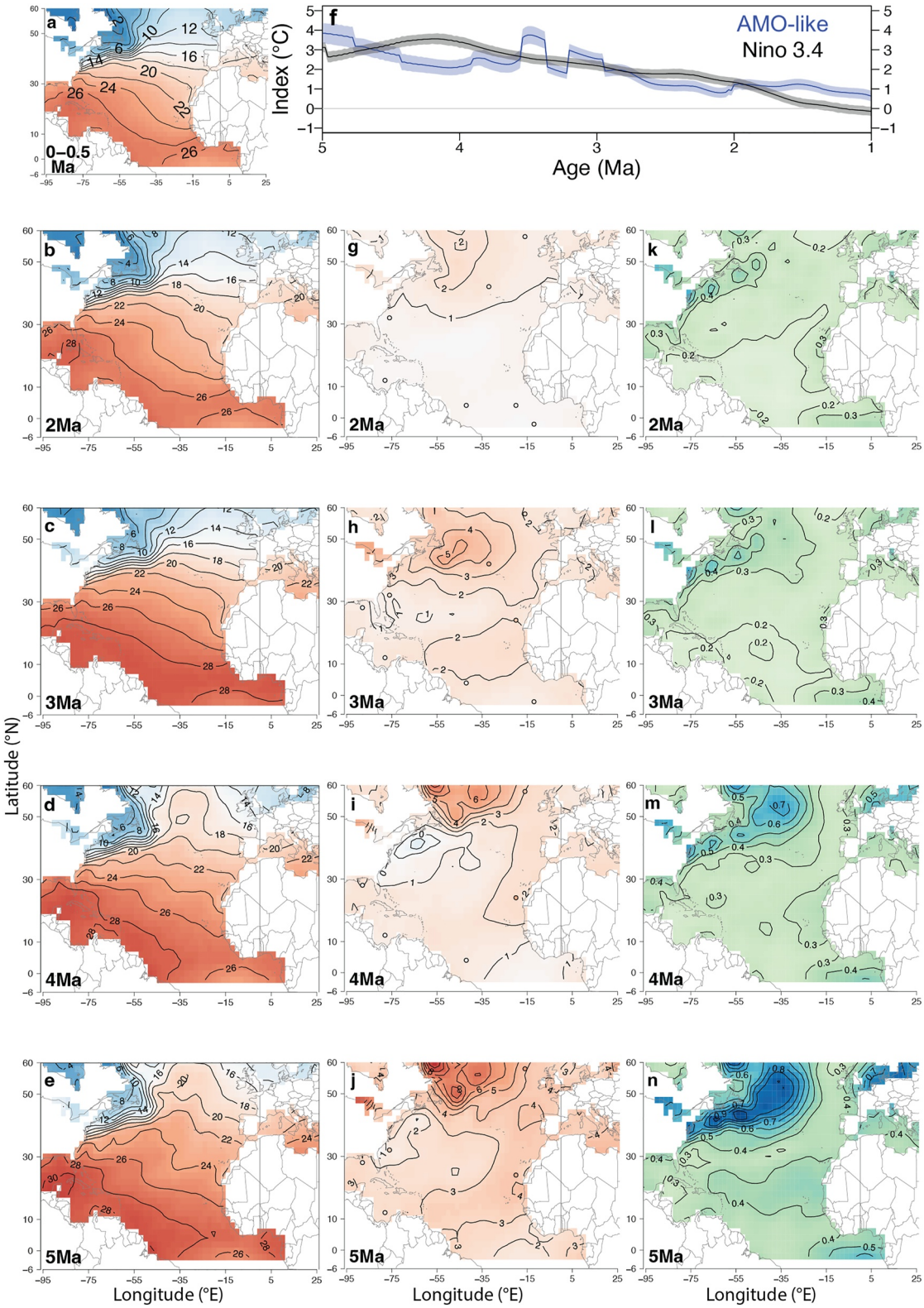
a
0–0.5 Ma
f
AMO-like
Nino 3.4
Index (°C)
Age (Ma)
b
2Ma
g
2Ma
k
2Ma
c
3Ma
h
3Ma
l
3Ma
d
4Ma
i
4Ma
m
4Ma
e
5Ma
j
5Ma
n
5Ma
Latitude (°N)
Longitude (°E)
Longitude (°E)
Longitude (°E)

Figure 6.

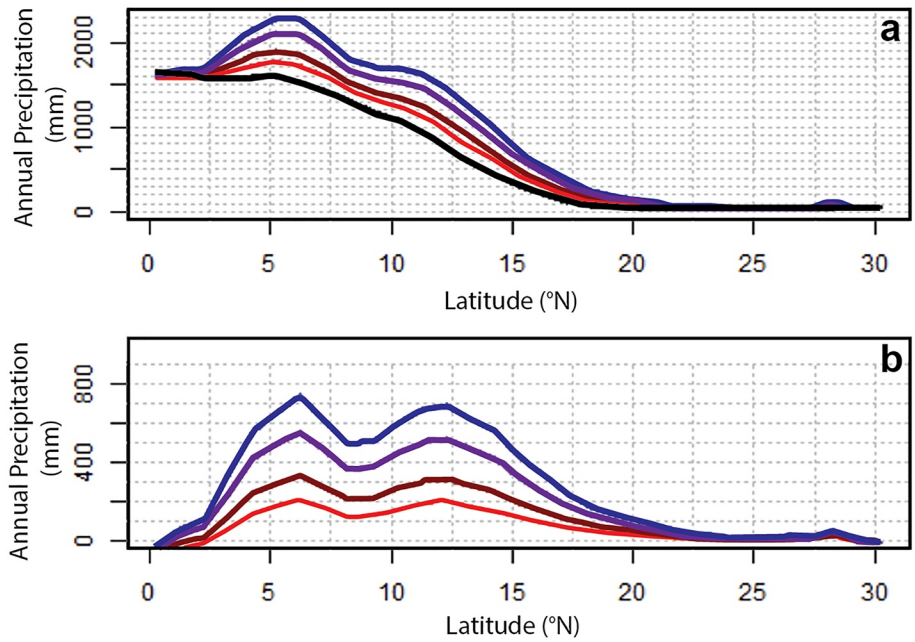

Figure 7. North-south profiles of zonally averaged precipitation Africa between 20°W and 35°E (a) for modern-day climatology (black) and calculated for 2 Ma (red), 3 Ma (brown), 4 Ma (purple), and 5 Ma (blue), and (b) calculated differences between past and present-day precipitation, with the same color coding.

of univariate calibrations (Nürnberg et al., 1996; Kısakürek et al., 2008). The Evans et al. (2016) calibration reconstructs SSTs that are slightly cooler than the original reconstruction but are on average within 0.4°C of the original (Figures S3e–S3h in Supporting Information S1). The cooler SSTs are apparent in the reconstructed time series of average SST anomalies over the region (Figure S4 in Supporting Information S1), but this AMO-like index is only <0.1°C–0.4°C lower than that of the original (Figure 6f). Overall, the different Mg/Ca_{sw} corrections reconstruct SSTs that are indistinguishable from one another.

4.5. Pliocene Sahel Rainfall

Today a relatively narrow zone separates the arid Sahara from the less arid Sahel to its south; the zonally averaged mean annual precipitation, between 20°W and 35°E, drops from ~1,100 mm at 10°N to ~350 mm at 15°N, and to only ~40 mm at 29°N (Figures 7 and 8). Much evidence, based on sediment deposited off the coast of West Africa, suggests that in Pliocene time this transition zone lay several degrees north of its current position. Using cores from several ODP sites near the coast of West Africa, Tiedemann et al. (1989) inferred that aridity in West Africa has increased since 7.4 Ma and particularly after ~4 Ma. They relied on dust derived from desert regions that lie inland from the humid coast. Dust accumulation accelerated first at sites in the south (ODP Sites 661 (9.35°N, 19.38°W) and 659 (18.08°N, 21.03°W)), and then after 4 Ma, but synchronously, rates of dust accumulation more than doubled at these and at Sites 660 (10.02°N, 19.23°W) and 658 (20.75°N, 18.58°W). From fossil pollen deposited at ODP Site 658, Leroy and Dupont (1994, 1997) inferred that wetter conditions prevailed before 3.5 Ma than since (Vallé et al., 2014). Leroy and Dupont (1994) reported that mangrove swamps and tropical forests lay east of Site 658, 5°N of their northern limit today, and therefore the rainfall needed to sustain them reach at least 5°N of the present location. Their observations appear to apply only to the coast of West Africa, where such swamps and forests exist.

Figure 6. (a) Maps of the average sea-surface temperatures (SSTs) for the base period (0–0.5 Ma) and (b–e) the reconstructed SSTs at 2, 3, 4, and 5 Ma. (f) Plio-Pleistocene time series of Atlantic multidecadal oscillation-like and Nino3.4 indices, the latter of which is presented in Wycech et al. (2020), calculated from principal component analysis (PCA) reconstructions at 0.02 Ma intervals. The shading on each time series is one standard error from the PCA reconstruction. (g–j) Reconstructed SST anomalies for 2, 3, 4, and 5 Ma. Anomalies were defined relative to the base period average SST for each smoothed record. Colors in circles show the proxy-based SST anomaly at each site using the same color scale as in the maps. (k–n) Maps of the standard errors calculated from 500 ensembles of each Principal Component (see Section 3.1 for details).

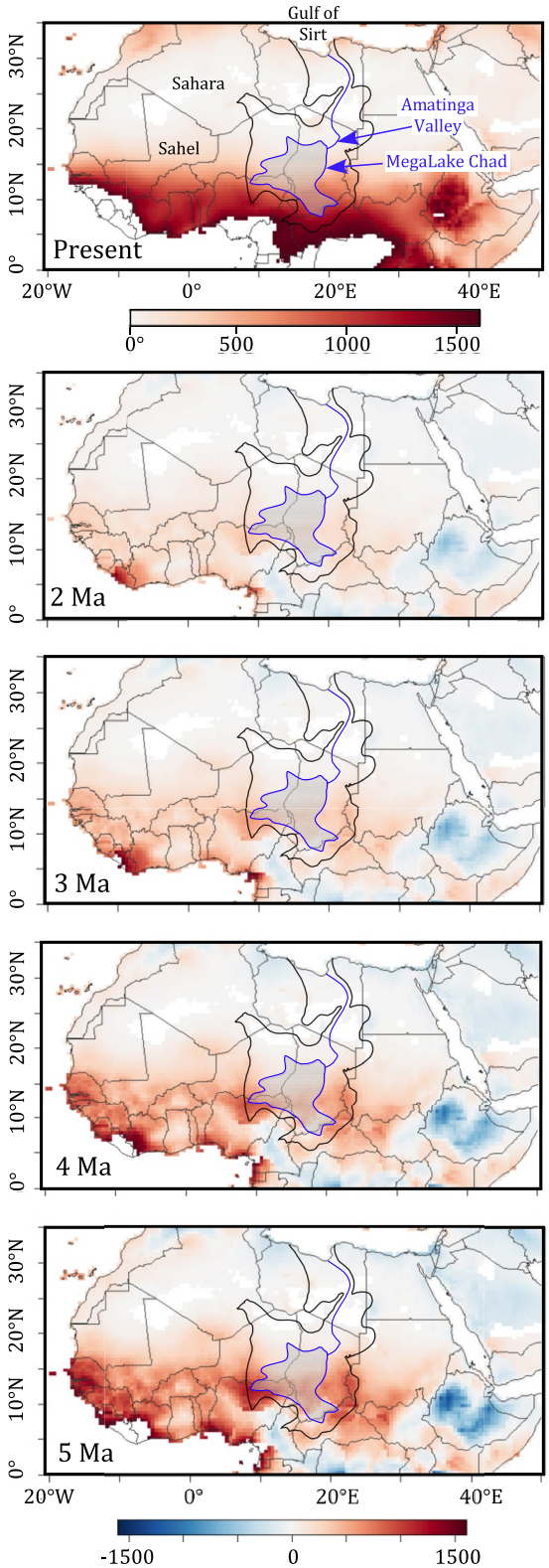
Gulf of
Sirt
Sahara
Sahel
Amatinga
Valley
MegaLake Chad
Present
2 Ma
3 Ma
4 Ma
5 Ma
30°N
20°N
10°N
0°
20°W
0°
20°E
40°E
0°
500
1000
1500
-1500
0
1500

Figure 8.

With the goal of assessing how a warmer Atlantic Ocean in Pliocene time might have affected surrounding climate, we regressed the Nino3.4 and AMO-like indices, which quantify SST distributions in tropical Pacific and North Atlantic regions, against rainfall anomalies over northern Africa during the contemporary period (e.g., Molnar & Rajagopalan, 2020). Most of the rain over North Africa, and over the Megalake Chad Basin, falls during the summer monsoon, during the northward march of the ITCZ (e.g., Adam et al., 2016a, 2016b). Although the cross-equatorial temperature gradient forces the ITCZ movement, we found that a regression model using AMO and Nino3.4 indices captures most of the rainfall variability over North Africa, and that correlations of rainfall with SSTs south of the equator are statistically insignificant (figure not shown). Although the regression model relies upon the modern SST-precipitation relationship, its application to the Pliocene provides a first-order approximation of rainfall over the African Sahel. Thus, we use this regression model, exploited also by Molnar and Rajagopalan (2020).

Using the estimates of those indices in the regressions for past times, we estimated differences in rainfall relative to climatology of the modern period over northern Africa (Figures 7 and 8). These differences show decreasing precipitation over much of the Sahel and more importantly over the Lake Chad basin since 5 Ma, with the smallest differences between present-day precipitation and that at 2 Ma. Zonal averages of precipitation show a decrease from 5 to 2 Ma in the latitudinal region of ∼2.5°N to 20°N (Figure 7a). Furthermore, since 5 Ma the location of rainfall gradient has shifted ∼4°–5° southward. A warmer North Atlantic seems to contribute an important part in this shift, as inferred for Holocene time (Molnar & Rajagopalan, 2020). Between 10°N and 15°N in the Sahara-Sahel region, the calculated annual rainfall decreased from ∼600 mm/year more than that today at 5 Ma to about 200 mm/year more at 2 Ma (Figure 7b). This result is consistent with PlioMIP2 GCM and CO_2-forcing simulations, which both indicate the Pliocene African Sahel was wetter than modern (Burls & Fedorov, 2017; Feng et al., 2022). Our methodology to reconstruct precipitation suggests SST differences in the Atlantic can account for a substantial decrease in rainfall since 5 Ma, and therefore have impacted hydrology, ecology, and the atmospheric circulation.

5. Implications for North African Rainfall

A wealth of evidence suggests that a huge lake, Megalake Chad, occupied the Chad Basin in the late Miocene and Pliocene (Figure 8). This evidence includes fossils of freshwater fish as large as 1 m in length (Otero et a l., 2009a, 2009b, 2010, 2011; Vignaud et al., 2002); widespread lacustrine sediments (Moussa et al., 2016); phytoliths and diatoms (Novello et al., 2015); fossils of a late Miocene extinct anthracotheriid Libycosaurus, an hippopotamus-like ungulate (Lihoreau et al., 2006); fossil mammals such as elephants, primates, equids, bovids, and rodents (Vignaud et al., 2002); trace fossils of burrowing animals (Duringer et al., 2000; Schuster et al., 2009); and aquatic birds (Louchart et al., 2004).

Griffin (2006) estimated that the area of Megalake Chad was ∼700,000 km^2, and therefore occupied 28% of a 2,500,000-km^2 basin (Schuster et al., 2009). In late Miocene and perhaps into early Pliocene time, the Megalake seems to have drained into the Mediterranean (e.g., Gladstone et al., 2007; Griffin, 2002, 2006; Lihoreau et al., 2006). The northward flowing river passed through Libya to the Gulf of Sirt in the Mediterranean. Griffin (2006) showed a satellite image of a now-dry meandering river valley, the Amatinga Valley, through the area north of Megalake Chad (Figure 8). Lihoreau et al. (2006) used the similarity of fossils of the Libycosaurus in Lake Chad Basin with others in the Sirt Basin in northern Libya as evidence of an aquatic connection. Drake et al. (2008) inferred that the region west of the river valley also contained vast lakes from Late Miocene time until ∼3 Ma. Using a GCM of the atmosphere, Gladstone et al. (2007) simulated an annual outflow of 2.1×10^{15} L carried by the river draining Megalake Chad in late Miocene time, when the lake was at its fullest, which would require an average rainfall of ∼800 mm/yr merely to sustain that flow.

There seems little doubt that the wettest period was in the late Miocene. Schuster et al. (2006), in fact, suggested that the Sahara Desert began to form at 7 Ma. Whether northward drainage of Megalake Chad continued into Pliocene time is not clear. Griffin (2006) inferred, largely from indirect evidence, that a "drawdown phase of

Figure 8. Climatology of annual precipitation rate (mm/yr, years averaged over 1951 to 2016) and calculated differences in North African rainfall at 2, 3, 4, and 5 Ma. Calculated precipitation anomalies at 2, 3, 4, and 5 Ma are based on regressions of modern rainfall against the Niño3.4 index and the Atlantic multidecadal oscillation (AMO) index, and then from estimates of those indices at 2, 3, 4, and 5 Ma. We use the Pliocene Niño3.4 index from Wycech et al. (2020) and the AMO-like index from this study (Figure 6f). Also labeled are features discussed in the text. The black line surrounding MegaLake Chad shows the boundary of its Mio-Pliocene drainage basin as given by Griffin (2006).

the river" occurred between ~5.8 and 5.3 Ma, and that northward flow terminated at 4.6 Ma. The presence of late Miocene, but not Pliocene, Libycosaurus species in both the Lake Chad and Sirt Basins agrees with wetter late Miocene than early Pliocene conditions. Fossil pollen indicate a "wooded humid habitat" if not rainforest, and little grass at ~7 Ma (Bonnefille, 2010), yielding to savanna-like grasslands between ~6 and 3 Ma (Zazzo et al., 2000), with gallery forests at 3.0–3.5 Ma adjacent to the lake (Brunet et al., 1995). Moreover, Zazzo et al. (2000) interpreted $\delta^{13}C$ values in Late Miocene and early Pliocene fossil tooth enamel as evidence of expanding savanna-like grasslands between ~6 and 3 Ma. Similarly, Otero et al. (2011) inferred a gradual increase in salinity in Megalake Chad between 7 and 3.6 Ma from increasing values of $\delta^{18}O$ in teeth of freshwater fish. We infer from these observations that Megalake Chad decreased in average size from 5 to 3 Ma, and may be a bit since then.

We ought not ignore that a large lake 350,000 km^2 in area (e.g., Schuster et al., 2005), and therefore roughly half the size of the Miocene megalake, occupied a large fraction of the Lake Chad Basin in Holocene time. That Holocene lake, however, drained southward into the Niger River and then into the South Atlantic (e.g., Armitage et al., 2015; Burke, 1976; Ghienne et al., 2002; Leblanc et al., 2006). Thus, the hypsometry of the Chad Basin has changed since Pliocene time. As important, large lakes may have waxed and waned throughout the past few million years in response to orbital variations in insolation (e.g., Kuechler et al., 2018; Leroy & Dupont, 1994; Trauth et al., 2008). Thus, it seems possible that even the Miocene Megalake Chad was ephemeral on 40,000-year periods.

The calculated differences between past and present-day rainfall over northern Africa (Figure 8) show decreasing precipitation over much of the Sahel and more importantly over the Lake Chad basin since 5 Ma. Using a crude resolution of rainfall, we calculate a present-day mean annual rainfall of 450 mm over the Chad Basin, 30% greater than the 350 mm estimated by Kutzbach (1980). Our calculations call for greater precipitation over the basin at 5, 4, 3, and 2 Ma by 375, 280, 168, and 105 mm/yr, respectively, or by 83%, 62%, 37%, and 23% more than 450 mm/yr. Several aspects of our estimates of greater Pliocene than present-day rainfall make them likely to be underestimates. First, the regressions that we use account for at most 64% of modern rainfall variability (e.g., Molnar & Rajagopalan, 2020). Second, the lake itself can affect rainfall on adjacent terrain, and GCM runs that include a Lake Chad show enhanced summer rainfall east of the lake (e.g., Coe & Bonan, 1997; Contoux et al., 2013; Krinner et al., 2012). Such runs also show a reduced rainfall over the lake, because convection there is suppressed, with some GCM runs suggesting that the total effect of the lake is small (e.g., Contoux et al., 2013), and others large (e.g., Krinner et al., 2012). Third, with greater vegetative cover of the surroundings, ground water flow can supply the lake while also preventing evaporation (e.g., Pham-Duc et al., 2020). We conclude that the effect of a warmer Pliocene than present-day North Atlantic on circulation over northern Africa played a major role in sustaining the Megalake Chad that characterized Pliocene, and perhaps Miocene time, but we cannot demonstrate that warmth alone accounts for existence of the size of the lake. We, nevertheless, draw attention to the fact that two indices—AMO and NINO3.4—in a simple linear regression model can produce a large part of the wetness over North Africa, and offers potential for further refinement.

6. Conclusion

A multiproxy reduced dimension methodology on two new Mg/Ca-based SST records and previously published Pliocene North Atlantic (2°S to 60°N) SST records spanning 5–0 Ma were used to reconstruct spatial and temporal images of North Atlantic SSTs that resemble that of a modern warm AMO phase. Relative to base period (0–0.5 Ma) conditions, warmest local SSTs occurred at ~5 Ma with the most extreme warming in the tropical and eastern subtropical North Atlantic and Labrador Sea. On a larger scale, North Atlantic SSTs have gradually cooled from a maximum at 5 Ma (AMO-like index = 3.8°C) toward base period conditions. The warm North Atlantic SSTs reconstructed in this study are likely not unique to the region during this time period as previous studies suggest global SSTs were warmer in the Pliocene (e.g., Dowsett & Robinson, 2009) primarily due to greenhouse gas forcing.

An added value of our approach is that it results in high spatial resolution maps ($2° \times 2°$) of SST anomalies, which provide for calculations of climate indices such as AMO and estimates of temperature/precipitation anomalies in distal regions teleconnected to North Atlantic SSTs. We estimate Pliocene rainfall over the African Sahel and Megalake Chad basin, based on the AMO-like index and NINO3.4 index (from Wycech et al., 2020). Our results

indicate northern Africa was close to twice as wet in the early Pliocene as today, which might have been sufficient to sustain Megalake Chad.

Data Availability Statement

Contemporary SST data used for the PCA is available at https://iridl.ldeo.columbia.edu/SOURCES/.NOAA/.NCDC/.ERSST/.version3b/.sst/. Proxy and SST records used in this study are available in Carlson et al. (2008), Groeneveld (2005), Herbert et al. (2010), Herbert et al. (2016), Herbert and Schuffert (1998), Hönisch et al. (2009), Lawrence et al. (2009), Lawrence et al. (2010), O'Brien et al. (2014), Pflaumann et al. (1998), Zhang et al. (2013), and Ziegler et al. (2008), Tables S1 and S2, and the Zenodo data repository (Wycech et al., 2022). Data analysis was performed in R (R Core Team, 2014), and the codes are also available through Zenodo (Wycech et al., 2022). The data set is licensed via Creative Commons Attribution 4.0 International without access conditions.

Acknowledgments
Funding provided by the CIRES Visiting Postdoctoral Fellowship (Wycech). We thank John Morton, Anne Jennings, and Payton Birdsong for technical assistance and Yochanan Kushnir for fruitful discussion. This research used samples provided by ODP. ODP was funded through the National Science Foundation (NSF) and participating countries under the management of Joint Oceanographic Institutions (JOI), Inc.

References

Adam, O., Bischoff, T., & Schneider, T. (2016a). Seasonal and interannual variations of the energy flux equator and ITCZ. Part I: Zonally averaged ITCZ position. *Journal of Climate*, *29*(9), 3219–3230. https://doi.org/10.1175/JCLI-D-15-0512.1

Adam, O., Bischoff, T., & Schneider, T. (2016b). Seasonal and interannual variations of the energy flux equator and ITCZ. Part II: Zonally varying shifts of the ITCZ. *Journal of Climate*, *29*(20), 7281–7293. https://doi.org/10.1175/JCLI-D-15-0710.1

Allen, K., Hönisch, B., Eggins, S. M., Haynes, L. L., Rosenthal, Y., & Yu, J. (2016). Trace element proxies for surface ocean conditions: A synthesis of culture calibrations with planktic foraminifera. *Geochimica et Cosmochimica Acta*, *193*, 197–221. https://doi.org/10.1016/j.gca.2016.08.015

Anand, P., Elderfield, H., & Conte, M. H. (2003). Calibration of Mg/Ca thermometry in planktonic foraminifera from a sediment trap time series. *Paleoceanography*, *18*(2), 1–15. https://doi.org/10.1029/2002PA000846

Armitage, S. J., Bristow, C. S., & Drake, N. A. (2015). West African monsoon dynamics inferred from abrupt fluctuations of Lake Mega-Chad. *Proceedings of the National Academy of Sciences*, *112*(28), 8543–8548. https://doi.org/10.1073/pnas.1417655112

Arnold, N., & Tziperman, E. (2015). Reductions in mid-latitude upwelling-favorable winds implied by weaker large-scale Pliocene SST gradients. *Paleoceanography*, *30*(1), 27–39. https://doi.org/10.1002/2015PA002806

Barreiro, M., Philander, G., Pacanowski, R., & Fedorov, A. (2006). Simulations of warm tropical conditions with application to middle Pliocene atmospheres. *Climate Dynamics*, *26*(4), 349–365. https://doi.org/10.1007/s00382-005-0086-4

Berntell, E., Zhang, Q., Chafik, L., & Körnich, H. (2018). Representation of multidecadal Sahel rainfall variability in 20th century reanalyses. *Scientific Reports*, *8*(1), 10937. https://doi.org/10.1038/s41598-018-29217-9

Bonnefille, R. (2010). Cenozoic vegetation, climate changes and hominid evolution in tropical Africa. *Global and Planetary Change*, *72*(4), 390–411. https://doi.org/10.1016/j.gloplacha.2010.01.015

Boyle, E. A., & Keigwin, L. D. (1985). Comparison of Atlantic and Pacific paleochemical records for the last 215,000 years: Changes in deep ocean circulation and chemical inventories. *Earth and Planetary Science Letters*, *76*(1–2), 135–150. https://doi.org/10.1016/0012-821X(85)90154-2

Boyle, E. A., & Rosenthal, Y. (1996). Chemical hydrography of the South Atlantic during the last glacial maximum: Cd vs. $\delta^{13}C$. In G. Wefer, W. H. Berger, G. Siedler, & D. J. Webb (Eds.), *The South Atlantic: Present and past circulation* (pp. 423–443). Springer.

Brassell, S. C., Eglinton, G., Marlowe, I. T., Pflaumann, U., & Sarnthein, M. (1986). Molecular stratigraphy: A new tool for climatic assessment. *Nature*, *320*(6058), 129–133. https://doi.org/10.1038/320129a0

Brunet, M., Beauvilain, A., Coppens, Y., Heintz, E., Moutaye, A. H. E., & Pilbeam, D. (1995). The first australopithecine 2500 kilometres west of the Rift Valley (Chad). *Nature*, *378*(6554), 273–275. https://doi.org/10.1038/378273a0

Burke, K. (1976). The Chad Basin: An active intra-continental basin. *Tectonophysics*, *36*, 197–206. https://doi.org/10.1016/B978-0-444-41549-3.50018-9

Burls, N. J., & Fedorov, A. V. (2017). Wetter subtropics in a warmer world: Contrasting past and future hydrological cycles. *Proceedings of the National Academy of Sciences*, *114*(49), 12888–12893. https://doi.org/10.1073/pnas.1703421114

Carlson, A. E., Stoner, J. S., Donnelly, J. P., & Hillaire-Marcel, C. (2008). Response of the southern Greenland Ice Sheet during the last two deglaciations. *Geology*, *36*(5), 359–362. https://doi.org/10.1130/G24519A.1

Carré, M., Sachs, J. P., Purca, S., Schauer, A. J., Braconnot, P., Falcón, R. A., et al. (2014). Holocene history of ENSO variance and asymmetry in the eastern tropical Pacific. *Science*, *345*(6200), 1045–1048. https://doi.org/10.1126/science.1252220

Chandan, D., & Peltier, W. R. (2018). On the mechanisms of warming the mid-Pliocene and the inference of a hierarchy of climate sensitivities with relevance to the understanding of climate futures. *Climate of the Past*, *14*(6), 825–856. https://doi.org/10.5194/cp-14-825-2018

Chandler, M., Rind, D., & Thompson, R. (1994). Joint investigation of the middle Pliocene climate II: GISS GCM Northern Hemisphere results. *Global and Planetary Change*, *9*(3–4), 197–219. https://doi.org/10.1016/0921-8181(94)90016-7

Chen, X., & Tung, K.-K. (2018). Global-mean surface temperature variability: Space-time perspective from rotated EOFs. *Climate Dynamics*, *51*(5–6), 1719–1732. https://doi.org/10.1007/s00382-017-3979-0

Clement, A. C., Seager, R., & Cane, M. A. (2000). Suppression of El Niño during the mid-Holocene by changes in the Earth's orbit. *Paleoceanography*, *15*(6), 731–737. https://doi.org/10.1029/1999PA000466

Coe, M. T., & Bonan, G. B. (1997). Feedbacks between climate and surface water in northern Africa during the middle Holocene. *Journal of Geophysical Research*, *102*(D10), 11087–11101. https://doi.org/10.1029/97JD00343

Collins, C. A., Castro, C. G., Asanuma, H., Rago, T. A., Han, S.-K., Durazo, R., & Chavez, F. P. (2002). Changes in the hydrography of central California waters associated with the 1997–98 El Niño. *Progress in Oceanography*, *54*(1–4), 129–147. https://doi.org/10.1016/S0079-6611(02)00046-0

Contoux, C., Jost, A., Ramstein, G., Sepulchre, P., Krinner, G., & Schuster, M. (2013). Megalake Chad impact on climate and vegetation during the late Pliocene and the mid-Holocene. *Climate of the Past*, *9*(4), 1417–1430. https://doi.org/10.5194/cp-9-1417-2013

Dekens, P. S., Lea, D. W., Pak, D. K., & Spero, H. J. (2002). Core top calibration of Mg/Ca in tropical foraminifera: Refining paleotemperature estimation. *Geochemistry, Geophysics, Geosystems*, *3*(4), 1022–1029. https://doi.org/10.1029/2001GC000200

Dekens, P. S., Ravelo, A. C., & McCarthy, M. D. (2007). Warm upwelling regions in the Pliocene warm period. *Paleoceanography*, *22*(3), PA3211. https://doi.org/10.1029/2006PA001394

Deser, C., Alexander, M. A., Xie, S.-P., & Phillips, A. S. (2010). Sea Surface temperature variability: Patterns and mechanisms. *Annual Review of Marine Science*, *2*(1), 115–143. https://doi.org/10.1146/annurev-marine-120408-151453

Donders, T. H., Wagner, F., Dilcher, D. L., & Visscher, H. (2005). Mid- to late-Holocene El Niño-Southern Oscillation dynamics reflected in the subtropical terrestrial realm. *Proceedings of the National Academy of Sciences*, *102*, 10904–10908. https://doi.org/10.1073/pnas.0505015102

Dowsett, H. (2007). The PRISM palaeoclimate reconstruction and Pliocene sea-surface temperature. In M. Williams, A. M. Haywood, F. J. Gregory, & D. N. Schmidt (Eds.), *Deep- time perspectives on climate change: Marrying the signal from computer models and biological proxies* (pp. 459–480). The Micropalaeontological Society.

Dowsett, H., Barron, J., & Poore, R. (1996). Middle Pliocene sea surface temperatures: A global reconstruction. *Marine Micropaleontology*, *27*(1–4), 13–25. https://doi.org/10.1016/0377-8398(95)00050-X

Dowsett, H. J., Cronin, T. M., Poore, R. Z., Thompson, R. S., Whatley, R. C., & Wood, A. M. (1992). Micropaleontological evidence for increased meridional heat transport in the North Atlantic ocean during the Pliocene. *Science*, *258*(5085), 1133–1135. https://doi.org/10.1126/science.258.5085.1133

Dowsett, H. J., & Robinson, M. M. (2009). Mid-Pliocene equatorial Pacific sea surface temperature reconstruction: A multi-proxy perspective. *Philosophical Transactions of the Royal Society A*, *367*(1886), 109–125. https://doi.org/10.1098/rsta.2008.0206

Dowsett, H. J., Robinson, M. M., Haywood, A. M., Hill, D. J., Dolan, A. M., Stoll, D. K., et al. (2012). Assessing confidence in Pliocene sea surface temperatures to evaluate predictive models. *Nature Climate Change*, *2*(5), 365–371. https://doi.org/10.1038/nclimate1455

Drake, N. A., El-Hawat, A. S., Turner, P., Armitage, S. J., Salem, M. J., White, K. H., & McLaren, S. (2008). Palaeohydrology of the Fazzan Basin and surrounding regions: The last 7 million years. *Palaeoceanography, Palaeoclimatology, Palaeoecology*, *263*(3–4), 131–145. https://doi.org/10.1016/j.palaeo.2008.02.005

Duringer, P., Brunet, M., Cambefort, Y., Beauvilain, A., Mackaye, H. T., Vignaud, P., & Schuster, M. (2000). Des boules de bousiers fossiles et leurs terriers dans les sites à Australopithèques du Pliocène inférieure tchadien. *Bulletin de la Societe Geologique de France*, *161*(2), 259–269. https://doi.org/10.2113/171.2.259

Ely, L. L. (1997). Response of extreme floods in the southwestern USA to climatic variations in the late Holocene. *Geomorphology*, *19*(3–4), 175–201. https://doi.org/10.1016/S0169-555X(97)00014-7

Ely, L. L., Enzel, Y., Baker, V. R., & Cayan, D. R. (1993). A 5000-year record of extreme floods and climate change in the southwestern United States. *Science*, *262*(5132), 410–412. https://doi.org/10.1126/science.262.5132.410

Enfield, D. B., Mestas-Nuñez, A. M., Mayer, D. A., & Cid-Serrano, L. (1999). How ubiquitous is the dipole relationship in tropical Atlantic sea surface temperatures? *Journal of Geophysical Research*, *104*(C4), 7841–7848. https://doi.org/10.1029/1998JC900109

Enfield, D. B., Mestas-Nuñez, A. M., & Trimble, P. J. (2001). The Atlantic multidecadal oscillation and its relation to rainfall and river flows in the continental U.S. *Geophysical Research Letters*, *28*(10), 2077–2080. https://doi.org/10.1029/2000GL012745

Evans, D., Brierley, C., Raymo, M., Erez, J., & Müller, W. (2016). Planktic foraminifera shell chemistry response to seawater chemistry: Pliocene–Pleistocene seawater Mg/Ca, temperature and sea level change. *Earth and Planetary Science Letters*, *438*(C), 139–148. https://doi.org/10.1016/j.epsl.2016.01.013

Fedorov, A. V., Dekens, P. S., McCarthy, M., Ravelo, A. C., de Menocal, P. B., Barreiro, M., et al. (2006). The Pliocene paradox (mechanisms for a permanent El Niño). *Science*, *312*(5779), 1485–1489. https://doi.org/10.1126/science.1122666

Feng, R., Bhattacharya, T., Otto-Bliesner, B. L., Brady, E. C., Haywood, A. M., Tindall, J. C., et al. (2022). Past terrestrial hydroclimate sensitivity controlled by Earth system feedbacks. *Nature Communications*, *13*(1), 1–11. https://doi.org/10.1038/s41467-022-28814-7

Folland, C. K., Palmer, T. N., & Parker, D. E. (1986). Sahel rainfall and worldwide sea temperatures, 1901–85. *Nature*, *320*(6063), 602–607. https://doi.org/10.1038/320602a0

Frischknecht, M., Münnich, M., & Gruber, N. (2015). Remote versus local influence of ENSO on the California current system. *Journal of Geophysical Research: Oceans*, *120*(2), 1353–1374. https://doi.org/10.1002/2014JC010531

Fu, M.-M., Cane, M. A., Molnar, P., & Tziperman, E. (2021). Wetter subtropics lead to reduced Pliocene coastal upwelling. *Paleoceanography and Paleoclimatology*, *36*(10), 1–22. https://doi.org/10.1029/2021PA004243

Gelman, A., & Hill, J. (2006). *Data analysis using regression and multilevel/hierarchical models*. Cambridge University Press.

Ghienne, J.-F., Schuster, M., Bernard, A., Duringer, P., & Brunet, M. (2002). The Holocene giant Lake Chad revealed by digital elevation models. *Quaternary International*, *87*(1), 81–85. https://doi.org/10.1016/S1040-6182(01)00063-5

Gill, E. C., Rajagopalan, B., Molnar, P., & Marchitto, T. M. (2016). Reduced-dimension reconstruction of the equatorial Pacific SST and zonal wind fields over the past 10,000 years using Mg/Ca and alkenone records. *Paleoceanography*, *31*(7), 928–952. https://doi.org/10.1002/2016PA002948

Gill, E. C., Rajagopalan, B., Molnar, P. H., Kushnir, Y., & Marchitto, T. M. (2017). Reconstruction of Indian summer monsoon winds and precipitation over the past 10,000 years using equatorial Pacific SST proxy records. *Paleoceanography*, *32*(2), 195–216. https://doi.org/10.1002/2016PA002971

Gladstone, R., Flecker, R., Valdes, P., Lunt, D., & Markwick, P. (2007). The Mediterranean hydrologic budget from a Late Miocene global climate simulation. *Palaeogeography, Palaeoclimatology, Palaeoecology*, *251*(2), 254–267. https://doi.org/10.1016/j.palaeo.2007.03.050

Gray, W. R., & Evans, D. (2019). Nonthermal influences on Mg/Ca in planktonic foraminifera: A review of culture studies and application to the last glacial maximum. *Paleoceanography and Paleoclimatology*, *34*(3), 306–315. https://doi.org/10.1029/2018pa003517

Green, B., Marshall, J., & Donohoe, A. (2017). Twentieth century correlations between extratropical SST variability and ITCZ shifts: AMO, PDO, and ITCZ variability. *Geophysical Research Letters*, *44*(17), 9039–9047. https://doi.org/10.1002/2017GL075044

Griffin, D. L. (2002). Aridity and humidity: Two aspects of the late Miocene climate of North Africa and the Mediterranean. *Palaeogeography, Palaeoclimatology, Palaeoecology*, *182*(1–2), 65–91. https://doi.org/10.1016/S0031-0182(01)00453-9

Griffin, D. L. (2006). The late Neogene Sahabi rivers of the Sahara and their climatic and environmental implications for the Chad Basin. *Journal of the Geological Society*, *163*(6), 905–921. https://doi.org/10.1144/0016-76492005-04

Groeneveld, J. (2005). *Effect of the Pliocene closure of the Panamanian Gateway on Caribbean and east Pacific sea surface temperatures and salinities by applying combined Mg/Ca and $\delta^{18}O$ measurements (5.6–2.2 Ma) (doctoral dissertation), Macau (00001516)*. University of Kiel. Retrieved from https://oceanrep.geomar.de/id/eprint/207

Harada, N., Handa, N., Harada, K., & Matsuoka, H. (2001). Alkenones and particulate fluxes in sediment traps from the central equatorial Pacific. *Deep-Sea Research*, *48*(3), 891–907. https://doi.org/10.1016/s0967-0637(00)00077-7

Hastings, D. W., Russell, A. D., & Emerson, S. R. (1998). Foraminiferal magnesium in *Globeriginoides sacculifer* as a paleotemperature proxy. *Paleoceanography*, *13*(2), 161–169. https://doi.org/10.1029/97pa03147

Haywood, A. M., Tindall, J. C., Dowsett, H. J., Dolan, A. M., Foley, K. M., Hunter, S. J., et al. (2020). The Pliocene Model Intercomparison Project Phase 2: Large-scale climate features and climate sensitivity. *Climate of the Past*, *16*(6), 2095–2123. https://doi.org/10.5194/cp-16-2095-2020

Herbert, T. D., Lawrence, K. T., Tzanova, A., Peterson, L. C., Caballero-Gill, R., & Kelly, C. S. (2016). Late Miocene global cooling and the rise of modern ecosystems. *Nature Geoscience*, *9*(11), 843–847. https://doi.org/10.1038/ngeo2813

Herbert, T. D., Peterson, L. C., Lawrence, K. T., & Liu, Z. (2010). Tropical ocean temperatures over the past 3.5 million years. *Science*, *328*(5985), 1530–1534. https://doi.org/10.1126/science.1185435

Herbert, T. D., & Schuffert, J. D. (1998). Alkenone unsaturation estimates of late Miocene through late Pliocene sea-surface temperatures at Site 958. In *Proceedings of the Ocean Drilling Program Scientific Results* (Vol. *159T*, pp. 17–21). Retrieved from http://www-odp.tamu.edu/publications/159t_sr/CHAPTERS/CHAP_02.PDF

Hönisch, B., Hemming, N. G., Archer, D., Siddall, M., & McManus, J. F. (2009). Atmospheric carbon dioxide concentration across the mid-pleistocene transition. *Science*, *324*(5934), 1548–1551. https://doi.org/10.1126/science.1171477

Hurrell, J. W., & Deser, C. (1997). North Atlantic climate variability: The role of the North Atlantic oscillation. *Journal of Marine Systems*, *79*(3–4), 231–244. https://doi.org/10.1016/j.jmarsys.2009.11.002

Hurrell, J. W., Kushnir, Y., Ottersen, G., & Visbeck, M. (2003). An overview of the North Atlantic oscillation. In J. W. Hurrell, Y. Kushnir, G. Ottersen, & M. Visbeck (Eds.), *The North Atlantic Oscillation: Climatic significance and environmental impact (geophysical monograph 124)* (pp. 1–35). American Geophysics Union.

Joyce, J. E., Tjalsma, L. R. C., & Prutzman, J. M. (1990). High-resolution planktic stable isotope record and spectral analysis for the last 5.35 M.Y.: Ocean Drilling Program Site 625, northeast Gulf of Mexico. *Paleoceanography*, *5*(4), 507–529. https://doi.org/10.1029/pa005i004p00507

Kienast, M., Kienast, S. S., Calvert, S. E., Eglinton, T. I., Mollenhauer, G., François, R., & Mix, A. C. (2006). Eastern Pacific cooling and Atlantic overturning circulation during the last deglaciation. *Nature*, *443*(7113), 846–849. https://doi.org/10.1038/nature05222

Kısakürek, B., Eisenhauer, A., Böhm, F., Garbe-Schonberg, D., & Erez, J. (2008). Controls on shell Mg/Ca and Sr/Ca in cultured planktonic foraminiferan, *Globigerinoides ruber* (white). *Earth and Planetary Science Letters*, *273*(3–4), 260–269. https://doi.org/10.1016/j.epsl.2008.06.026

Knox, J. C. (2000). Sensitivity of modern and Holocene floods to climate change. *Quaternary Science Reviews*, *19*(1–5), 439–457. https://doi.org/10.1016/s0277-3791(99)00074-8

Koutavas, A., de Menocal, P. B., Olive, G. C., & Lynch-Stieglitz, J. (2006). Mid-Holocene El Niño-Southern Oscillation (ENSO) attenuation revealed by individual foraminifera in eastern tropical Pacific sediments. *Geology*, *34*(12), 993–996. https://doi.org/10.1130/g22810a.1

Krinner, G., Lézine, A.-M., Braconnot, P., Sepulchre, P., Ramstein, G., Grenier, C., & Gouttevin, I. (2012). A reassessment of lake and wetland feedbacks on the North African Holocene climate. *Geophysical Research Letters*, *39*(7), L07701. https://doi.org/10.1029/2012GL050992

Kuechler, R. R., Dupont, L. M., & Schefuß, E. (2018). Hybrid insolation forcing of Pliocene monsoon dynamics in West Africa. *Climate of the Past*, *14*(1), 73–84. https://doi.org/10.5194/cp-14-73-2018

Kutzbach, J. E. (1980). Estimates of past climates at paleolake Chad, North Africa, based on a hydrological and energy-balance model. *Quaternary Research*, *14*(2), 210–223. https://doi.org/10.1016/0033-5894(80)90049-6

Lawrence, K. T., Herbert, T. D., Brown, C. M., Raymo, M. E., & Haywood, A. M. (2009). High-amplitude variations in North Atlantic sea surface temperature during the early Pliocene warm period. *Paleoceanography*, *24*(2), 1–15. https://doi.org/10.1029/2008pa001669

Lawrence, K. T., Sosdian, S., White, H. E., & Rosenthal, Y. (2010). North Atlantic climate evolution through the Plio-Pleistocene climate transitions. *Earth and Planetary Science Letters*, *300*(3–4), 329–342. https://doi.org/10.1016/j.epsl.2010.10.013

Lea, D. W., Mashiotta, T. A., & Spero, H. J. (1999). Controls on magnesium and strontium uptake in planktonic foraminifera determined by live culturing. *Geochimica et Cosmochimica Acta*, *63*(16), 2369–2379. https://doi.org/10.1016/S0016-7037(99)00197-0

Leblanc, M., Favreau, G., Maley, J., Nazoumou, Y., Leduc, C., Stagnitti, F., et al. (2006). Reconstruction of Megalake Chad using shuttle radar topographic Mission data. *Palaeogeography, Palaeoclimatology, Palaeoecology*, *239*(1–2), 16–27. https://doi.org/10.1016/j.palaeo.2006.01.003

Leduc, G., Schneider, R., Kim, J., & Lohmann, G. (2010). Holocene and Eemian sea surface temperature trends as revealed by alkenone and Mg/Ca paleothermometry. *Quaternary Science Reviews*, *29*(7–8), 989–1004. https://doi.org/10.1016/j.quascirev.2010.01.004

Leroy, S., & Dupont, L. (1994). Development of vegetation and continental aridity in northwestern Africa during the Late Pliocene: The pollen record of ODP site 658. *Palaeoclimatology, Palaeogeography, Palaeoecology*, *109*(2–4), 295–316. https://doi.org/10.1016/0031-0182(94)90181-3

Leroy, S., & Dupont, L. M. (1997). Marine palynology of the ODP site 658 (N-W Africa) and its contribution to the stratigraphy of late Pliocene. *Geobios*, *30*(3), 351–359. https://doi.org/10.1016/s0016-6995(97)80194-5

Li, Z.-Y., Luo, Y.-C., Arnold, N., & Tziperman, E. (2019). Reductions in strong upwelling-favorable wind events in the Pliocene. *Paleoceanography and Paleoclimatology*, *34*(12), 1931–1944. https://doi.org/10.1029/2019PA003760

Lihoreau, F., Boisserie, J.-R., Viriot, L., Coppens, Y., Likius, A., Mackaye, H. T., et al. (2006). Anthracotheres dental anatomy reveals a late Miocene Chado-Libyan bioprovince. *Proceedings of the National Academy of Sciences*, *103*(23), 8763–8767. https://doi.org/10.1073/pnas.0603126103

Liu, Y., & Chiang, J. C. H. (2012). Coordinated abrupt weakening of the Eurasian and North African monsoons in the 1960s and links to extratropical North Atlantic cooling. *Journal of Climate*, *25*(10), 3532–3548. https://doi.org/10.1175/jcli-d-11-00219.1

Locarnini, R. A., Mishonov, A. V., Antonov, J. I., Boyer, T. P., Garcia, H. E., Baranova, O. K., et al. (2010). World Ocean Atlas 2009, volume 1: Temperature. In S. Levitus (Ed.), *NOAA Atlas NESDIS 68* (p. 184). U.S. Government Printing Office.

Louchart, A., Mourer-Chauvire, C., Mackaye, H. T., Likius, A., Vignaud, P., & Brunet, M. (2004). Les oiseaux du Pliocène inférieure du Djourab, Tchad, Afrique centrale. *Bulletin de la Societe Geologique de France*, *175*(4), 413–421. https://doi.org/10.2113/175.4.413

Marchitto, T. M. (2006). Precise multielemental ratios in small foraminiferal samples determined by sector field ICP-MS. *Geochemistry, Geophysics, Geosystems*, *7*(5), Q05P13. https://doi.org/10.1029/2005gc001018

Marlow, J. R., Lange, C. B., Wefer, G., & Rosell-Melé, A. (2000). Upwelling intensification as a part of the Pliocene-Pleistocene climate transition. *Science*, *290*(5500), 2288–2291. https://doi.org/10.1126/science.290.5500.2288

Marlowe, I. T., Brassell, S. C., Eglinton, G., & Green, J. C. (1984). Long chain unsaturated ketones and esters in living algae and marine sediments. *Organic Geochemistry*, *6*, 135–141. https://doi.org/10.1016/0146-6380(84)90034-2

Marshall, J., Kushnir, Y., Battisti, D., Chang, P., Czaja, A., Dickson, R., et al. (2001). North Atlantic climate variability: Phenomena, impacts and mechanisms. *International Journal of Climatology*, *21*(15), 1863–1898. https://doi.org/10.1002/joc.693

Martin, E. R., Thorncroft, C., & Booth, B. B. B. (2014). The multidecadal Atlantic SST—Sahel rainfall teleconnection in CMIP5 simulations. *Journal of Climate*, *27*(2), 784–806. https://doi.org/10.1175/JCLI-D-13-00242.1

Martínez, I., Keigwin, L., Barrows, T. T., Yokoyama, Y., & Southon, J. (2003). La Niña-like conditions in the eastern equatorial Pacific and a stronger Choco jet in the northern Andes during the last glaciation. *Paleoceanography*, *18*(2), 1033. https://doi.org/10.1029/2002PA000877

Medina-Elizalde, M., Lea, D. W., & Fantle, M. S. (2008). Implications of seawater Mg/Ca variability for Plio-Pleistocene tropical climate reconstruction. *Earth and Planetary Science Letters*, *269*(3–4), 585–595. https://doi.org/10.1016/j.epsl.2008.03.014

Miller, M. D., & Tziperman, E. (2017). The effect of changes in surface winds and ocean stratification on coastal upwelling and sea surface temperatures in the Pliocene. *Paleoceanography*, *32*(4), 371–383. https://doi.org/10.1002/2016PA002996

Molnar, P., & Cane, M. A. (2002). El Niño's tropical climate and teleconnections as a blueprint for pre-Ice Age climates. *Paleoceanography*, *17*(2), 1021. https://doi.org/10.1029/2001PA000663

Molnar, P., & Cane, M. A. (2007). Early Pliocene (pre-ice age) El Niño-like global climate: Which El Niño? *Geosphere*, *3*(5), 337–365. https://doi.org/10.1130/ges00103.1

Molnar, P., & Rajagopalan, B. (2012). Late Miocene upward and outward growth of eastern Tibet and decreasing monsoon rainfall over the northwestern Indian subcontinent since ∼10 Ma. *Geophysical Research Letters*, *39*(9), L09702. https://doi.org/10.1029/2012GL051305

Molnar, P., & Rajagopalan, B. (2020). Mid-Holocene Sahara-Sahel Precipitation from the vantage of present-day climate. *Geophysical Research Letters*, *47*(16), e2020GL088171. https://doi.org/10.1029/2020GL088171

Moussa, A., Novello, A., Lebatard, A.-E., Decarreau, A., Fontaine, C., Barboni, D., et al. (2016). Lake Chad sedimentation and environments during the late Miocene and Pliocene: New evidence from mineralogy and chemistry of the Bol core sediments. *Journal of African Earth Sciences*, *118*, 192–204. https://doi.org/10.1016/j.jafrearsci.2016.02.023

Moy, C. M., Seltzer, G. O., Rodbell, D. T., & Anderson, D. M. (2002). Variability of El Niño/southern oscillation activity at millennial timescales during the Holocene epoch. *Nature*, *420*(6912), 162–165. https://doi.org/10.1038/nature01194

Müller, P., & Fischer, G. (2001). A 4-year sediment trap record of alkenones from the filamentous upwelling region off Cape Blanc, NW Africa and a comparison with distributions in underlying sediments. *Deep Sea Research Part I: Oceanographic Research Papers*, *48*(8), 1877–1903. https://doi.org/10.1016/S0967-0637(00)00109-6

Müller, P., Kirst, G., Gotz, R., von Storch, I., & Rosell-Mele, A. (1998). Calibration of the alkenone paleotemperature index $U^{K'}_{37}$ based on core-tops from the eastern South Atlantic and the global ocean (60°N–60°S). *Geochimica et Cosmochimica Acta*, *62*(10), 1757–1772. https://doi.org/10.1016/s0016-7037(98)00097-0

Nezlin, N. P., & McWilliams, J. C. (2003). Satellite data, empirical orthogonal functions, and the 1997–1998 El Niño off California. *Remote Sensing of Environment*, *84*(2), 234–254. https://doi.org/10.1016/s0034-4257(02)00109-8

Novello, A., Lebatard, A.-E., Moussa, A., Barboni, D., Sylvestre, F., Bourlès, D. L., et al. (2015). Diatom, phytolith, and pollen records from a $^{10}Be/^{9}Be$ dated lacustrine succession in the Chad basin: Insight on the Miocene–Pliocene paleoenvironmental changes in Central Africa. *Palaeogeography, Palaeoclimatology, Palaeoecology*, *430*, 85–103. https://doi.org/10.1016/j.palaeo.2015.04.013

Nürnberg, D., Bijma, J., & Hemleben, C. (1996). Assessing the reliability of magnesium in foraminiferal calcite as a proxy for water mass temperatures. *Geochimica et Cosmochimica Acta*, *60*(5), 803–814. https://doi.org/10.1016/0016-7037(95)00446-7

O'Brien, C. L., Foster, G. L., Martínez-Botí, M. A., Abell, R., Rae, J. W. B., & Pancost, R. D. (2014). High sea surface temperatures in tropical warm pools during the Pliocene. *Nature Geoscience*, *7*(8), 606–611. https://doi.org/10.1038/ngeo2194

Ohkouchi, N., Kawamura, K., Kawahata, H., & Okada, H. (1999). Depth ranges of alkenone production in the central Pacific Ocean. *Ocean Biogeochemical Cycles*, *13*(2), 695–704. https://doi.org/10.1029/1998GB900024

Okada, H. (2000). Neogene and quaternary calcareous nannofossils from the Blake Ridge, sites 994, 995, and 997. In C. K. Paull, R. Matsumoto, P. J. Wallace, & W. P. Dillon (Eds.), *Proceedings of the Ocean Drilling Program, Scientific Results* (pp. 331–341). Ocean Drilling Program.

Otero, O., Lécuyer, C., Fourel, F., Martineau, F., Mackaye, H. T., Vignaud, P., & Brunet, M. (2011). Freshwater fish $\delta^{18}O$ indicates a Messinian change of the precipitation regime in Central Africa. *Geology*, *39*(5), 435–438. https://doi.org/10.1130/G31212.1

Otero, O., Pinton, A., Mackaye, H. T., Likius, A., Vignaud, P., & Brunet, M. (2009a). First description of a Pliocene ichthyofauna from Central Africa (site KL2, Kolle area, Eastern Djurab, Chad): What do we learn? *Journal of African Earth Sciences*, *54*(3–4), 62–74. https://doi.org/10.1016/j.jafrearsci.2009.03.004

Otero, O., Pinton, A., Mackaye, H. T., Likius, A., Vignaud, P., & Brunet, M. (2009b). Fishes and palaeogeography of the African drainage basins: Relationships between Chad and neighbouring basins throughout the Mio-Pliocene. *Palaeogeography, Palaeoclimatology, Palaeoecology*, *274*(3–4), 134–139. https://doi.org/10.1016/j.palaeo.2009.01.005

Otero, O., Pinton, A., Mackaye, H. T., Likius, A., Vignaud, P., & Brunet, M. (2010). The early/late Pliocene ichthyofauna from Koro-Toro, Eastern Djurab, Chad. *Geobios*, *43*(2), 241–251. https://doi.org/10.1016/j.geobios.2009.10.003

Pahnke, K., Sachs, J. P., Keigwin, L., Timmermann, A., & Xie, S.-P. (2007). Eastern tropical Pacific hydrologic changes during the past 27, 000 years from D/H ratios in alkenones. *Paleoceanography*, *22*(4), PA4214. https://doi.org/10.1029/2007PA001468

Paull, C. K., Matsumoto, R., Wallace, P. J., & Dillon, W. P. (1996). Site 997. In *Proceedings of the Ocean Drilling Program, Scientific Results* (pp. 277–334). Ocean Drilling Program.

Pearson, P. N., Ditcheld, P. W., Singano, J., Harcourt-Brown, K. G., Nicholas, C. J., Shackleton, N. J., & Hall, M. A. (2001). Warm tropical sea surface temperatures in the Late Cretaceous and Eocene epochs. *Nature*, *415*(6855), 481–487. https://doi.org/10.1038/35097000

Pearson, P. N., Van Dongen, B. E., Nicholas, C. J., Pancost, R. D., Schouten, S., Singano, J. M., & Wade, B. S. (2007). Stable warm tropical climate through the Eocene Epoch. *Geology*, *35*(3), 211–214. https://doi.org/10.1130/g23175a.1

Pflaumann, U., Sarnthein, M., Ficken, K., Grothmann, A., & Winkler, A. (1998). Variations in eolian and carbonate sedimentation, sea-surface temperature, and productivity over the last 3 M.Y. at Site 958 off Northwest Africa. In J. V. Firth (Ed.), *Proceedings of the Ocean Drilling Program, Scientific Results* (pp. 3–16). Ocean Drilling Program. Retrieved from http://www-odp.tamu.edu/publications/159t_sr/chapters/CHAP_01.PDF

Pham-Duc, B., Sylvestre, F., Papa, F., Frappart, F., Bouchez, C., & Crétaux, J.-F. (2020). The Lake Chad hydrology under current climate change. *Scientific Reports*, *10*(1), 5498. https://doi.org/10.1038/s41598-020-62417-w

Rabinowitz, P. D., Merrell, W. J., Garrison, L. E., & Kidd, R. B. (1985). *Leg 100 report*. Ocean Drilling Program.

Rae, J. W. B., Sarnthein, M., Foster, G. L., Ridgwell, A., Grootes, P. M., & Elliott, T. (2014). Deep water formation in the North Pacific and deglacial CO_2 rise. *Paleoceanography*, *29*(6), 645–667. https://doi.org/10.1002/2013PA002570

Rausch, S., Bohm, F., Bach, W., Klugel, A., & Eisenhauer, A. (2012). Calcium carbonate veins in ocean crust record a threefold increase of seawater Mg/Ca in the past 30 million years. *Earth and Planetary Science Letters*, *362*, 215–224. https://doi.org/10.1016/j.epsl.2012.12.005

Ravelo, A. C., & Andreasen, D. H. (1999). Using planktonic foraminifera as monitors of the tropical surface ocean. In F. Abrantes & A. C. Mix (Eds.), *Reconstructing Ocean History*. Springer. https://doi.org/10.1007/978-1-4615-4197-4_14

R Core Team. (2014). R: A language and environment for statistical computing [Software]. R Foundation for Statistical Computing, Vienna. Retrieved from https://www.R-project.org/

Rebotim, A., Voelker, A. H. L., Jonkers, L., Waniek, J. J., Meggers, H., Schiebel, R., et al. (2017). Factors controlling the depth habitat of planktonic foraminifera in the subtropical eastern North Atlantic. *Biogeosciences*, *14*(4), 827–859. https://doi.org/10.5194/bg-14-827-2017

Regenberg, M., Regenberg, A., Garbe-Schönberg, D., & Lea, D. W. (2014). Global dissolution effects on planktonic foraminiferal Mg/Ca ratios controlled by the calcite-saturation state of bottom waters. *Paleoceanography*, *19*(3), 1–16. https://doi.org/10.1002/2013pa002492

Robinson, M. M., Dowsett, H. J., Dwyer, G. S., & Lawrence, K. T. (2008). Reevaluation of mid-Pliocene North Atlantic sea surface temperatures. *Paleoceanography*, *23*(3), PA3213. https://doi.org/10.1029/2008pa001608

Rodbell, D. T., Seltzer, G. O., Anderson, D. M., Abbott, M. B., Enfield, D. B., & Newman, J. H. (1999). An ~15,000-year record of El Niño-driven alluviation in southwestern Ecuador. *Science*, *283*(5401), 516–520. https://doi.org/10.1126/science.283.5401.516

Sandweiss, D. H., Richardson, J. B., III, Reitz, E. J., Rollins, H. B., & Maasch, K. A. (1996). Geoarcheological evidence from Peru for a 5000 years B.P. onset of El Niño. *Science*, *273*(5281), 1531–1533. https://doi.org/10.1126/science.273.5281.1531

Sandweiss, D. H., Solis, R. S., Moseley, M. E., Keefer, D. K., & Ortloff, C. R. (2009). Environmental change and economic development in coastal Peru between 5,800 and 3,600 years ago. *Proceedings of the National Academy of Sciences*, *106*(5), 1359–1363. https://doi.org/10.1073/pnas.0812645106

Schuster, M., Duringer, P., Ghienne, J.-F., Roquin, C., Sepulchre, P., Moussa, A., et al. (2009). Chad basin: Paleoenvironments of the Sahara since the late Miocene. *Comptes Rendus Geoscience*, *341*(8–9), 603–611. https://doi.org/10.1016/j.crte.2009.04.001

Schuster, M., Duringer, P., Ghienne, J.-F., Vignaud, P., Mackaye, H. T., Likius, A., & Brunet, M. (2006). The age of the Sahara Desert. *Science*, *311*(5362), 821. https://doi.org/10.1126/science.1120161

Schuster, M., Roquin, C., Duringer, P., Brunet, M., Caugy, M., Fontugne, M., et al. (2005). Holocene lake Mega-Chad palaeoshorelines from space. *Quaternary Science Reviews*, *24*(16–17), 1821–1827. https://doi.org/10.1016/j.quascirev.2005.02.001

Sexton, P. F., Wilson, P. A., & Pearson, P. N. (2006). Microstructural and geochemical perspectives on planktic foraminiferal preservation: "Glassy" versus "Frosty". *Geochemistry, Geophysics, Geosystems*, *7*(12), 1–29. https://doi.org/10.1029/2006gc001291

Shukla, S. P., Chandler, M. A., Rind, D., Sohl, L. E., Jonas, J., & Lerner, J. (2011). Teleconnections in a warmer climate: The Pliocene perspective. *Climate Dynamics*, *37*(9–10), 1869–1887. https://doi.org/10.1007/s00382-010-0976-y

Smith, T. M., Reynolds, R. W., Peterson, T. C., & Lawrimore, J. (2008). Improvements to NOAA's historical merged land–ocean surface temperature analysis (1880–2006). *Journal of Climate*, *21*(10), 2283–2296. https://doi.org/10.1175/2007JCLI2100.1

Spezzaferri, S., Kucera, M., Pearson, P. N., Wade, B. S., Rappo, S., Poole, C. R., et al. (2015). Fossil and genetic evidence for the polyphyletic Nature of the planktonic foraminifera *Globigerinoides*, and description of the New Genus *Trilobatus*. *PLoS One*, *10*(5), 1–20. https://doi.org/10.1371/journal.pone.0128108

Sutton, R. T., McCarthy, G. D., Robson, J., Sinha, B., Archibald, A. T., & Gray, L. J. (2018). Atlantic multidecadal variability and the UK ACSIS Program. *Bulletin of the American Meteorological Society*, *99*(2), 415–425. https://doi.org/10.1175/BAMS-D-16-0266.1

Thompson, D. W. J., Lee, S., & Baldwin, M. P. (2003). Atmospheric processes governing the northern hemisphere annular mode/North Atlantic oscillation. In J. W. Hurrell, Y. Kushnir, G. Ottersen, & M. Visbeck (Eds.), *The North Atlantic oscillation: Climatic significance and environmental impact (geophysical monograph 124)* (pp. 81–112). American Geophysical Union.

Tiedemann, R., Sarnthein, M., & Stein, R. (1989). Climatic changes in the western Sahara: Aeolo-marine sediment record of the last 8 million years (Sites 657–661). *Proceedings of the Ocean Drilling Program, Scientific Results*, *108*, 241–278.

Tierney, J. E., Haywood, A. M., Feng, R., Bhattacharya, T., & Otto-Bliesner, B. L. (2019). Pliocene warmth consistent with greenhouse gas forcing. *Geophysical Research Letters*, *46*(15), 9136–9144. https://doi.org/10.1029/2019GL083802

Tierney, J. E., & Tingley, M. P. (2018). BAYSPLINE: A New calibration for the alkenone paleothermometer. *Paleoceanography and Paleoclimatology*, *33*(3), 281–301. https://doi.org/10.1002/2017PA003201

Trauth, M. H., Larrasoaña, J. C., & Mudelsee, M. (2008). Trends, rhythms and events in Plio-Pleistocene African climate. *Quaternary Science Reviews*, *28*(5–6), 399–411. https://doi.org/10.1016/j.quascirev.2008.11.003

Trenberth, K. E., & Shea, D. J. (2005). Atlantic hurricanes and natural variability in 2005. *Geophysics Research Letters*, *33*(12), L12704. https://doi.org/10.1029/2006gl026894

Vallé, F., Dupont, L. M., Leroy, S. A. G., Schefuß, E., & Wefer, G. (2014). Pliocene environmental change in West Africa and the onset of strong NE trade winds (ODP Sites 659 and 658). *Palaeogeography, Palaeoclimatology, Palaeoecology*, *414*, 403–414. https://doi.org/10.1016/j.palaeo.2014.09.023

Vignaud, P., Duringer, P., Mackaye, H. T., Likius, A., Blondel, C., Boisserie, J.-R., et al. (2002). Geology and palaeontology of the Upper Miocene Toros-Menalla hominid locality, Chad. *Nature*, *418*(6894), 152–155. https://doi.org/10.1038/nature00880

Vizcaíno, M., Rupper, S., & Chiang, J. C. H. (2010). Permanent El Niño and the onset of Northern Hemisphere glaciations: Mechanism and comparison with other hypotheses. *Paleoceanography*, *25*(2), PA2205. https://doi.org/10.1029/2009PA001733

Volkman, J. K., Eglinton, G., Corner, E. D. S., & Forsberg, T. E. V. (1980). Long-chain alkenes and alkenones in the marine coccolithophorid *Emiliania huxleyi*. *Phytochemistry*, *19*(12), 2619–2622. https://doi.org/10.1016/S0031-9422(00)83930-8

Von Storch, H., & Zwiers, F. W. (2001). *Statistical analysis in climate research*. Cambridge University Press.

Wills, R. C. J., Armour, K. C., Battisti, D. S., & Hartmann, D. L. (2019). Ocean-atmosphere dynamical coupling fundamental to the Atlantic multidecadal oscillation. *Journal of Climate*, *32*(1), 251–272. https://doi.org/10.1175/jcli-d-18-0269.1

Wycech, J., Kelly, D. C., & Marcott, S. (2016). Effects of seafloor diagenesis on planktic foraminiferal radiocarbon ages. *Geology*, *44*(7), 551–554. https://doi.org/10.1130/G37864.1

Wycech, J., Rajagopalan, B., Molnar, P., Gill, E., & Marchitto, T. (2022). Multiproxy reconstruction of Pliocene North Atlantic sea surface temperatures and implications for rainfall in North Africa (version 1) [Dataset]. Zenodo. https://doi.org/10.5281/zenodo.6657931

Wycech, J. B. (2017). *Novel techniques and approaches to enhance the fidelity of foraminiferal paleoclimate records (doctoral dissertation)*. University of Wisconsin-Madison. Proquest 10623383.

Wycech, J. B., Gill, E., Rajagopalan, B., Marchitto, T. M., Jr., & Molnar, P. H. (2020). Multiproxy reduced-dimension reconstruction of Pliocene equatorial Pacific Sea Surface temperatures. *Paleoceanography and Paleoclimatology*, *35*(1), e2019PA003685. https://doi.org/10.1029/2019PA003685

Zazzo, A., Bocherens, H., Brunet, M., Beauvilain, A., Mackaye, H. T., Vignaud, P., & Mariotti, A. (2000). Herbivore paleodiet and paleoenvironmental changes in Chad during the Pliocene using stable isotope ratios of tooth enamel carbonate. *Paleobiology*, *26*(2), 294–309. https://doi.org/10.1666/0094-8373(2000)026<0294:hpapci>2.0.co;2

Zeebe, R. E., & Tyrrell, T. (2019). History of carbonate ion concentration over the last 100 million years II: Revised calculations and new data. *Geochimica et Cosmochimica Acta*, *257*, 373–392. https://doi.org/10.1016/j.gca.2019.02.041

Zhang, R. (2017). On the persistence and coherence of subpolar sea surface temperature and salinity anomalies associated with the Atlantic multidecadal variability. *Geophysical Research Letters*, *44*(15), 7865–7875. https://doi.org/10.1002/2017GL074342

Zhang, R., & Delworth, T. L. (2006). Impact of Atlantic multidecadal oscillations on India/Sahel rainfall and Atlantic hurricanes. *Geophysical Research Letters*, *33*(17), L17712. https://doi.org/10.1029/2006GL026267

Zhang, Y. G., Pagani, M., Liu, Z., Bohaty, S. M., & DeConto, R. (2013). A 40-million-year history of atmospheric CO_2. *Philosophical Transactions of the Royal Society A: Mathematical, Physical & Engineering Sciences*, *371*(2001), 20130096. https://doi.org/10.1098/rsta.2013.0096

Zhang, Z.-S., Li, X.-Y., Guo, C.-C., Otterå, O. H., Nisancioglu, K. H., Tan, N., et al. (2021). Mid-pliocene Atlantic meridional overturning circulation simulated in PlioMIP2. *Climate of the Past*, *17*(1), 529–543. https://doi.org/10.5194/cp-17-529-2021

Ziegler, M., Nürnberg, D., Karas, C., Tiedemann, R., & Lourens, L. J. (2008). Persistent summer expansion of the Atlantic Warm Pool during glacial abrupt cold events. *Nature Geoscience*, *1*(9), 601–605. https://doi.org/10.1038/ngeo277